CAPACITIVE PROBE FOR ICE DETECTION AND ACCRETION RATE MEASUREMENT: PROOF OF CONCEPT

By

Kwadwo Poku Owusu

A thesis submitted in partial fulfillment of the requirements for the degree of

Master of Science, Department of Mechanical Engineering

University of Manitoba

ABSTRACT

Ice accretion on wind turbines is a major problem in cold climates that reduces power generation and fatigues turbine components. Effective anti-icing and de-icing strategies to manage ice accretion require reliable local assessment of icing conditions and a measure of ice accretion rate on structures. Such sensors could be located on meteorological towers near wind farms or the nacelle of wind turbines. A new concept for the estimation of atmospheric ice accretion based on the measurement of capacitance and resistance change between two charged cylinders as ice accretes on the cylinders is introduced in this study. Numerical simulation of the electric field between the charged cylinders is used to investigate the dependence of the sensitivity of capacitance to the distance between the cylindrical probes and location of ice deposits. The numerical results are validated experimentally using aluminum probes and a set of acrylic cylindrical sleeves that fit over the probes to simulate icing with accurate geometries. A charged cylindrical probes system constructed based on the numerical results is described and evaluated under controlled rime and glaze icing conditions in the University of Manitoba Icing Wind Tunnel. Test results indicate ice builds up on the cylindrical probes and the measured capacitance increases while the resistance decreases. The change in measured capacitance change correlates well with the increase in the ice mass. Rime and glaze ice are distinguishable based on the rate of change of resistance with ice accretion. The numerical and experimental results provide a proof of concept of the charged cylindrical probes ice accretion measurement concept.

ACKNOWLEDGMENTS

My sincere gratitude goes to my advisors Dr. David C.S. Kuhn and Dr. Eric L. Bibeau for their supervision, support and encouragement throughout this research. Many thanks to Bruce Ellis, for thoroughly training me in the use of the wind icing tunnel as well helping me acquire data for this research. Many thanks to all my friends for lending a hand when needed. Last but the most, I am grateful to my parents and siblings for their unconditional love and support.

TABLE OF CONTENTS

LIST OF TABLES

LIST OF FIGURES

Chapter 1

Introduction

1.1 Background

Globally, fossil fuels are the primary source of electricity with nuclear power plants and hydropower being employed to meet the demands in certain regions of the world. In recent times, concerns about the harmful effects of emissions of carbon and global warming have created new demands for an alternative and suitable energy source such as wind energy. The benefits of wind energy include an abundant source, pollution free, local power generation at site that reduces long distances transmission losses [Patel, 2006] and economic gains such as investments in rural development as well as creation of new jobs.

In 2007, worldwide wind energy generation was estimated at 94 GW. It is projected that the global investment in the wind industry will reach $1 trillion by the year 2020, equivalent to 500 GW of electricity [CanWEA, 2008]. In Canada, wind power capacity is expected to rise from 0.4 GW in 2004 to 8.5 GW in 2020. This according to Natural Resources Canada represents 6% of the national generating capacity and 3.6% of total electricity production [CanWEA, 2007]. In 2006, the Province of Manitoba reiterated its commitment of harvesting 1 GW of wind power over the next decade [Rondeau, 2006]. However, there are problems associated with wind power generation in cold climates such as Canada, most notably icing. Icing can cause problems ranging from decrease of power due to modifications in the aerodynamics of the blades [Jasinski et al., 1998], aerodynamic changes of blade profile which results in increased blade vibration and fatigue of wind turbine components [Ganander and

Ronsten, 2003], to additional safety concerns to people and wildlife due to detachment of accumulated ice [Seifert, 2003].

These problems require prevention of ice adhering to the surface or removal of ice from the blades once accretion has occurred. Anti-icing and de-icing techniques are commonly mentioned in the literature as the means of ice mitigation. To effectively use anti-icing and de-icing techniques, the detection of the onset of the icing event is foremost. In the wind engineering industry, a number of methods have been devised to detect icing. These methods are categorised into two groups: direct and indirect methods. The direct methods are based on the principle of detecting a property change caused by the ice accretion. Examples of such properties include mass and dielectric constants. The inductance change probe of Lee and Seegmiller [1996], impedance change probe of Wallace et al., [2002] and the microwave ice detector of Magenheim [1977] are examples of ice detectors based on direct methods. The indirect methods involve detecting weather conditions such as humidity and temperature that lead to atmospheric icing conditions or detecting effects of icing, e.g. reduction in power generation or reduction in the speed of anemometers, with an empirical or deterministic model used to determine when icing is occurring [Homola et.al, 2006]. The reduction in the speeds of the heated and unheated anemometers of Craig and Craig [1995] and the noise generation frequency of Seifert [2003] are examples of the indirect methods.

In the work of Homola et al., [2006], most of the 29 methods presented were found not to be reliable for ice detection base on the study's set of requirements. These requirements include high sensitivity and wide area detection capabilities. However, they indicated that ice sensors based on the changes in electric properties such as capacitance and inductance probes appear promising for use in the detection of icing in the wind engineering industry. However, these

latter methods have not been scientifically investigated and assessed. Some of the reasons for this assertion include knowledge of electrical property changes and the ability of such a probe to detect icing over a wider area than at a single point. The latter is important because depending on the mechanism of the icing event, ice accretion would generally tend not to occur at a single point or location but rather at varying locations. For instance, glaze ice can accrete over a large area due to water run-off freezing in different locations.

1.2 Thesis objectives

There is a lack of knowledge as to whether a capacitance probe can be an effective method for ice detection. Although capacitance probes have been developed for other applications (two-phase gas-liquid flows), there is a clear lack in the literature how effective capacitance probes could be for ice detection. The objectives of this thesis are to:

1. Test the concept of estimation of atmospheric ice accretion on structures based on the measurement of capacitance and resistance change between two electrically charged cylindrical probes as ice accretes on the cylinders. The probes would be located on metrological towers near wind farms or the nacelle of wind turbines.

2. Use a theoretical model to study the changes in capacitance with ice accretion, and validate these studies in a laboratory setting using “modelled” ice growths.

3. Validate the charged cylindrical probes ice accretion measurement concept under simulated rime and glaze ice conditions in the University of Manitoba Icing Wind Tunnel.

Chapter 2

Literature survey

2.1 Introduction

This chapter reviews the following topics: general impact of icing, atmospheric icing, ice accretion process, methods of ice detection, icing sensors, general uses of capacitive sensors and the two-cylinder capacitance device.

2.2 General impact of icing

In the past, wind turbines were mainly installed along coastal areas where extreme cold temperatures that facilitate icing events do not occur or they had marginal importance on design parameters [Wolff, 2000]. Recently, there is growing interest to install wind turbines at sites prone to heavy icing events since there is large wind energy potential. Additionally, the rate of icing increases with elevation and with taller wind turbines, the tips of the blades are more likely to experience icing notwithstanding a location in a coastal area [Kimura et al., 2000]. With the potential for more humidity in the air, climate change may make the situation more prominent. Icing of wind turbine blades or other related components can lead to decreased power production, overproduction of power by the wind turbine at low temperatures (higher air density), increased fatigue loads or prolonged breaks in power production due to safety concerns such as detachment of ice from the turbine blades.

To maximise the performance of these wind turbines, meteorological instruments are generally mounted on meteorological towers to measure environmental parameters: humidity, ambient air temperature, wind speed and direction. Various research groups have studied the effects of icing

on these meteorological instruments. An example of such studies was done by Seifert [2003]. He studied the effect of winter conditions on two-cup anemometers — one heated and the other unheated, at Tauren Wind Park, Austria. His findings indicate differences in the wind speed recorded by the anemometers. This is consistent with most wind measurements in cold climates. The wind speed measured by the unheated anemometer was consistent with expected results, since there was no significant accumulation of ice on it. On the other hand, the heated anemometer collected ice, melted, with the resulting liquid water moving outwards due to centrifugal forces and refreezing at the tips. This increased the weight of the cups culminating in a reduction of the wind speed measured by this anemometer.

Ice storms can also be very destructive. This has increased the interest in icing research, particularly in developing reliable ice sensors/probes for mounting on meteorological towers. There are currently few ice sensors/probes commercially available, which are capable of detecting ice in addition to sensing ice accumulation rates (e.g. Goodrich ice sensor). However, there is presently no ice sensor available that can detect ice, distinguish between the two types of in-cloud icing and indicate the rate of icing. Therefore, the focus of this research is to demonstrate a novel concept for an ice sensor capable of detecting ice, indicating icing rate as well as distinguishing between the two types of in-cloud icing.

2.3 Atmospheric icing

Icing is the process by which snow or ice accretes on the surface of an object or a structure exposed to the atmosphere. In-cloud icing and precipitation icing are the two main types of atmospheric icing. In-cloud icing occurs when supercooled water drops impact on the surface of a structure resulting in the formation of ice. There are two types of in-cloud icing: rime and glaze

icing [Homola et al., 2006 & Drage and Lange, 2005]. In-cloud ice accretion on a structure is dependent on factors such as the wind speed, the dimensions of the exposed structure, the drop size distribution, the liquid water content in the air, surface conditions of the exposure structure and the air temperature [Frohboese et al., 2007 & Drage and Lange, 2005]. Precipitation icing occurs when snow or rain freezes on impact with the surface of a structure. Freezing rain, which differs from rime and glaze ice by virtue of its large drop size and wet snow, are the two types of precipitation icing [Homola et al., 2006 & Drage and Lange, 2005].

In keeping with the set of objectives of this research, icing wind tunnel experiments were focused on in-cloud icing. Moreover, in-cloud icing is the predominate form of icing which affects wind turbines [Kraj, 2007].

2.3.1 Glaze icing

Glaze icing occurs when supercooled water drops impact the surface of a structure at or below freezing temperatures under high liquid water content conditions. Glaze ice is typically characterised by water run-offs on the icing surface, since the impinging drops do not have enough time to freeze before the next drops impact the same area. Glaze ice growth is generally termed wet [COST 727, 2006]. It occurs at temperatures between -4°C and 0°C [Bose, 1992]. Glaze ice is transparent in appearance with horns-like impressions on its surface. The density of glaze ice typically ranges between 0.8 and 0.9 g/cm^3 [Wang, 2008], which is comparatively larger than rime ice as will be evident in the next section. Due to its higher density, glaze ice adheres firmly to the surface when formed. The following are factors that favour glaze ice formation: relatively large drop size distribution compared to rime ice, slow dissipation of the latent heat of

fusion, rapid accretion and low degree of supercooling. Figure 2.1 shows a photograph of glaze ice obtained on capacitance sensors.

Figure 2.1: A picture of glaze ice formed on the cylindrical probes

2.3.2 Rime icing

Rime ice is the most common type of in-cloud icing [Frohboese et al., 2007], and occurs when relatively small supercooled water drops impact the surface of a structure at colder temperatures than glace ice, and rapidly freeze, incorporating air gaps into it structure under low liquid water content conditions. Each impinging drop freezes before the next drop impacts the same area, and the ice growth is said to be dry [COST 727, 2006]. Rime ice typically forms at temperatures between -12°C and -4°C [Bose, 1992]. Rime ice is opaque and feathery in appearance. The density range is between 0.59 and 0.90 g/cm^3 [Wang, 2008], which is lower than that of glaze ice. As a result of its formation process, it adheres less tenaciously to the surface where it is formed, and damage due to rime ice is less than that due to glaze ice. The following are factors

that favour rime ice formation: rapid dissipation of the latent heat of fusion, high degree of supercooling, slow accretion and small drop size. A typical rime ice formation is depicted in Figure 2.2.

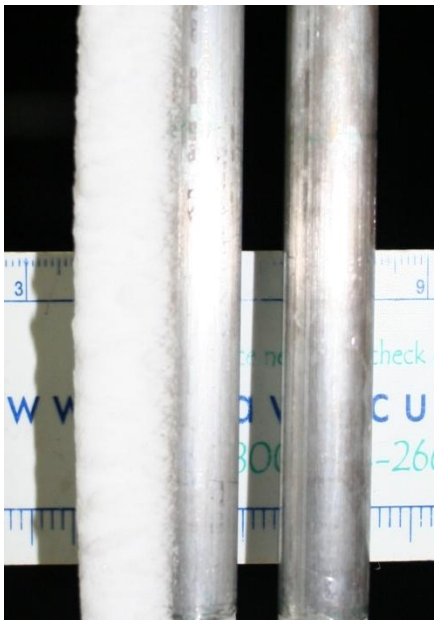

Figure 2.2: A typical rime ice formation on the cylindrical probes

2.4 Ice accretion process

Cloud drops, rain drops, snow or water vapour are the natural sources of ice accretion on the surface of structures. Cloud drops and rain drops differ in both size and fall (terminal) velocity, with cloud drops having a relatively smaller size as well as lower fall velocity [Makkonen, 2000]. Condensation of water vapour is generally negligible compared to normal accretion rates of ice due to the impact of supercooled water drops and snow particles on the surface of structures. This translates into large ice load formation due to particles or drops colliding with structures compared to condensation of water vapour into ice loads [Makkonen, 2000].

The rate of icing on a shape is governed by [Drage and Lange, 2005 & Makkonen, 2000]:

$$\frac{dM}{dt} = \alpha_1 \alpha_2 \alpha_3 FA \qquad [2.1]$$

where F is the flux density, that is, the product of the mass accumulation per unit volume w and the velocity v of the particles relative to the structure, A is the cross sectional area of the shape, and $\alpha_1, \alpha_2, \alpha_3$ are the collision, sticking and accretion efficiency, respectively.

2.4.1 Collision efficiency

Collision efficiency α_1, is the ratio of the flux density of the drops that impinges on the surface to the maximum flux density in the free stream. Collision efficiency is a function of the transport mechanism of the drops in the air stream. Molecular diffusion, Brownian motion, thermophoresis, turbulent diffusion and inertia impaction are possible transport mechanisms.

Molecular diffusion is the dominant transport mechanism for particles with sizes less than 0.1 μm. These particles follow the gas laws. Such particles tend to move with velocities close to those of the gas molecules as well as follow the streamlines of the gas flow [Reid, 1971].

Brownian motion is applicable to particles falling within the size interval of 0.1 to 1 μm. Brownian motion is characterised by the random motion of particles in the gas stream due to collision with the gas molecules [Reid, 1971].

Particles within the size interval of 0.1 to 5 μm when subject to a temperature gradient move toward the colder regions (i.e. down the temperature gradient) in a gas. Transportation of particles due to this force is known as thermophoresis. This phenomenon occurs because the gas molecules become more energetic on the hotter region pushing the particles towards the colder region. In addition to particle size, thermophoresis is dependent on factors such as the steepness

of the temperature gradient and the heat absorption ability of the particles [Piazza and Parola, 2008].

Within the turbulent flow regime, particles of size 1 to 10 μm are able to move across the laminar sub-layer to the surface of the structure. These particles achieve this fate by picking up higher kinetic energy from the gas eddies. This type of transport mechanism is known as turbulent diffusion [Reid, 1971].

With comparatively large particle sizes, inertia impaction transport mechanism dominates. Due to their large size and higher density than the surrounding carrier gas, they acquire enough momentum to move independently of local variations in the carrier gas, resulting in collision with the surface of obstacles [Reid, 1971]. The dominate transport mechanism of falling supercooled atmospheric water drops is inertia impaction.

As a supercooled water drop moves through the air stream, the probability of it impacting the surface of a structure due to inertia is a function of the drop size, the geometry of the structure and the flow field around the structure. The non-dimensional Stokes number characterises this probability and is define as the ratio of the stopping distance of a particle to a characteristic dimension of the obstacle. Particles with Stokes number greater than 1 will typically continue to move in a straight path impacting the structure in its way while the air stream moves around the structure. Particles with Stokes number less than 1 tend to follow the air stream [Crowe et al., 1998].

The collision efficiency is reduced from a maximum value of 1 when the Stokes number is less than 1. Additionally, collision efficiency is a function of the wind speed and the size of the impinging structure [Drage and Lange, 2005 & Makkonen, 2000]. Determination of the collision efficiency for non-simple structures is computationally expensive and complicated, since it

involves the numerical solution of both the airflow field and drop trajectories. However, for practical engineering applications, simplified approaches based on the assumption that the icing structure is cylindrical in shape are available [Makkonen, 2000].

2.4.2 Sticking efficiency

Sticking efficiency α_2, is the ratio of the flux density of drops that hit and stick to the surface of the structure to the flux density of the drops that hit the surface of the structure. Drops are considered trapped or stuck to the surface of a structure when they are permanently collected or their residence time is long enough to affect the rate of icing, for example, exchange heat with the surface [Makkonen, 2000]. It is reduced from a maximum value of 1 when drops are reflected or bounce off the surface of the structure. The sticking efficiency is assumed unity for in-cloud icing [Ahti, and Makkonen, 1982]. For wet snow, the sticking efficiency is approximately 1 [Makkonen, 2000] while for dry snow the sticking efficiency is approximately 0 [Wakahama et al., 1977]. Air temperature and humidity are known to affect the sticking efficiency [Makkonen, 2000].

2.4.3 Accretion efficiency

Accretion efficiency α_3, is the ratio of the rate of ice accretion in relation to the flux density of the drops that stick to the surface. Accretion efficiency has a maximum value of 1, when the heat flux from the accretion process is enough to cause sufficient freezing, thereby sticking drops all lead to ice accretion. Rime ice has an accretion efficiency of 1, since all the impinging water drops freeze upon impact with the exposed surface. Glaze ice however, has an accretion efficiency of less than 1 because the freezing rate is controlled by the rate at which the latent heat

released in the freezing process can be transferred away from the icing surface. To determine the accretion efficiency for a surface undergoing glaze icing, the budget of the heat transfer process occurring on the surface is paramount [Makkonen, 2000].

2.5 Methods of ice detection

Homola et al., [2005] reviewed 29 ice detection methods for use in the wind industry. These methods were discussed based on a set of requirements for a sensor/probe under broad operating conditions. The set requirements included the ability of a sensor/probe to detect icing over a wide surface area and high sensor/probe sensitivity. They separated these methods into two groups: direct method and indirect method. None of the sensors/probes considered performed satisfactorily but methods based on capacitance, impedance and infrared spectroscopy were concluded to hold promise.

2.5.1 Indirect methods of ice detection

The indirect methods of ice detection involve measuring weather conditions such as humidity, and temperature that lead to icing or detecting the effects of icing, for example, reduction in the power generated by the wind turbine or reduction in the speed of anemometers. Empirical or deterministic models are then used to determine when icing is occurring [Homola et al., 2006]. The reduction in the speeds of anemometers method of Craig and Craig [1995] and the noise generation frequency method of Seifert [2003] are typical examples of indirect methods. Homola et al., [2005], evaluated five indirect methods of ice detection and, no methods met the essential requirement of an ability to detect icing over a wide and representative surface area. See Appendix B for a list of indirect methods available in the literature.

2.5.2 Direct methods of ice detection

The direct methods of ice detection are based on the principle of detecting property changes caused by ice accretion. Examples of such properties include mass and dielectric constants. The inductance change probe of Lee and Seegmiller [1996], the impedance change probe of Wallace et al., [2002] and the microwave ice detector of Magenheim [1977] are examples of direct methods. Homola et al., [2006] evaluated twenty-four direct methods of ice detection and all the methods based on the change in an electrical property with ice accretion appear suitable for use in the wind industry. Besides their ability to detect icing over a wide surface area, they have low power consumptions. The advantages of using capacitive sensors are listed in Section 2.7.1. See Appendix B for a list of direct methods available in the literature.

2.6 Icing sensors

The development of a reliable ice detector for the wind industry is an active area of research. Presently, over six ice sensors/probes are available on the market. These sensors/probes were initially mainly intended for use in the aerospace industry. The most commonly used icing sensors/probes and recent methods reported in literature will now be presented.

2.6.1 Goodrich Ice Detector Models 0871LH1

The 0871LHI Ice Detector Model is a low power sensor manufactured by Goodrich Sensor Systems. The Goodrich Ice Detector Model 0871LH1 uses an ultrasonically vibrating probe to detect the presence of ice. As ice accrete on the probe during an icing event, the resonant frequency decreases as a result of the added mass of ice. The probe frequency is monitored by a sensor and software. The decrease in probe frequency is detected and reported by this software.

At the same time, the heating system of the probe is turned on until the frequency of the probe returns to the predetermined set point. To ensure complete de-icing, a delayed factor is incorporated [Goodrich 0871LH1, 2008].

Improper mounting may result in the collection of ice, which in time will cover the probe, hindering further detection of ice [Goodrich 0871LH1, 2008]. Additionally, this sensor is a single point ice detection device and cannot distinguish between the two types of in-cloud icing.

2.6.2 LID-3210C and LID-3210D Ice Detectors

Labkotec developed the LID-3210C and LID-3210 D Ice Detectors specifically for Arctic wind power plants and meteorological stations to detect icing weather conditions [Labkotec Ice Detectors LID 33210D, 2003 and Labkotec Ice Detectors LID 33210C, 2009].

These ice detectors use ultrasonic principles to detect icing conditions within time intervals between heating and cooling of a special wire sensor. Solid ice weakens the transmitted wave through the sensor wire more than water or any other non-solid substance. As soon as ice accretion is detected, the cylinder is heated via the heating element to rid the sensor wire of ice. Accumulation rate of ice is indicated by the frequency of the generated ice alarms.

One major defect of these ice detectors are their inability to melt all accumulated ice during an icing event, which may result in delayed ice detection [Labkotec Ice Detectors LID 33210D, 2003 and Labkotec Ice Detectors LID 33210C, 2009]. In addition, both devices are single point ice detection sensors.

2.6.3 METEO device

The METEO device was designed by EGU Brno, and is a monitoring device which when used in connection with communications systems, aids in the continuous measurement of ice mass. Additionally, wind velocity, temperature and wind direction can be outputted from this device [COST 727, 2006].

The METEO device consists of a collection of monitoring instruments. Each of these monitoring instruments is configured to the expected local weather conditions and, will report back warning message when the set values have been exceeded or when an abnormal event has occurred. The warning messages may include exceeding set mass limit and wind velocity [COST 727, 2006].

This device is not capable of detect icing over a wide area and distinguish between the two types of in-cloud icing.

2.6.4 Ice Monitor

The Ice Monitor is manufactured by SAAB Technologies, and was initially developed for power line surveillance systems. It measures mass of accumulated ice gravimetrically. The working element is a freely rotating steel pipe resting on a rod placed on load cells. As ice accretes on the freely rotating steel pipe, the ice load is weighed by the load cells [COST 727, 2006 and Laakso et al., 2003]. The Ice Monitor does not measure ice accumulation rate, and is not able to detect ice over a wide area in addition to not been capable of distinguish between the two types of in-cloud icing.

2.6.5 HoloOptics T20-series Ice Detectors

HoloOptics manufacture the T20-series. The T20-series Ice Detectors sense the presence of ice as well as measuring ice accretion rate. The working element comprise of either a single head or four heads with infrared emitter, a photo detector and a probe.

An icing event is recorded if more than 95% of the probe is covered with a 50 μm thick layer of glaze ice or a 90 μm thick layer of other types of ice. Once icing is detected, the probe's internal heating system is activated to melt the accreted ice. The time it takes to deice is dependent solely on the icing rate if sufficient amount of heating power is provided. The time lapse between icing events is used to determine the icing rate [Laakso et al., 2003]. These ice detectors do not distinguish between the two types of in-cloud icing.

2.6.6 Instrumar Limited Ice Sensor IM101

Instrumar Limited Ice Sensor IM101 measures both the surface temperature and electrical impedance of a ceramic probe. This data is then used to determine the surface conditions of the probe. An 'icing' signal is triggered when the parameters fall within the 'icing window' that is already programmed into the device. The probe has a solid-state switch, which closes when an icing event is indicated, and remains closed for a set time. The closure can be used to control devices such as heaters, alarms or even turn on/off power devices. There is limited information on this probe [Laakso et al., 2003].

2.6.7 Heated and unheated anemometers

As discussed earlier in Section 2.2, the measured wind speeds from a heated and unheated anemometer are different during an icing event. This difference can be used to identify an icing

event [Craig and Craig, 1995]. Concerns about this approach includes: the uncertainty of the speed difference between the unheated and heated anemometer for it to be interpreted as an icing event, the possibility of false alarms emanating from wakes on the top of the wind turbine nacelle and the longer time for a frozen standard unheated anemometer to deice, which can impede determining the actual time when an icing event begun [Homola et al., 2006, Craig and Craig, 1995 and Laakso et al., 2003].

2.6.8 Actual power generated versus predicted power from wind speed

The wind speed provided by the wind turbine nacelle anemometer can be used to compute the anticipated power produced by the wind turbine. This anticipated power compared with the actual power production from the wind turbine may provide a means of identifying an icing event. This is because as ice accretes on the blades of the wind turbine, there is a reduction in the power produced compared to the power curve. Concerns about this method include how small should the power degradations be and how soon after an icing event can this method be used. In addition, reduced power production can easily be attributed to "anemometer error" when in fact icing is the cause [Laakso et al., 2003].

2.7 General uses of capacitive sensors

Capacitive based sensors find applications in numerous fields. Examples of such applications include: measurement of instantaneous bulk void fraction in a vertical tube section [Rocha, 2009], void fraction measurement and flow pattern identification [Ahmed and Ismail, 2008], estimation of the soil water content through the measurement of relative permittivity

[Robinson et al., 1998], and measurement of oil film thickness between the piston ring and liner in internal combustion engines [Ducu et al., 2001].

In the wind and icing industries, capacitive based sensor applications includes measurement of density and velocity of falling snow [Louge et al., 1997], recording profiles of dielectric permittivity through dry snow [Louge et al., 1998] and detection of the presence of an icing event [e.g. Geraldi et. al., 1996].

2.7.1 Advantages of capacitive sensors

Some of the advantages of capacitance sensing probes are [Wimmer et al., 2007]:

- *No line-of-sight is required.* Capacitive sensors generate an electric field to detect the presence of dielectric materials. This electric field radiates outward around the probe and a dielectric material in close proximity of the field affects the measured capacitance. This attribute enables non-invasive measurements.
- *Reliable data collection and greater speed.* Analysis and post processing of data can be done using a microcontroller. The update rate of a capacitive sensor or probe is generally around 100 Hz. Faster data collection is possible; however, the signal-to-noise ratio decreases.
- *Inexpensive and easy to find components*. Capacitive sensors or probes are generally constructed from relatively few inexpensive and off-the-shelf components. The power consumption of such a sensor is generally low.
- *Smaller size and easily fit into integrated circuit or onto printed circuit boards (PC boards).* A capacitance sensor or probe of diameter 2 cm provides a sensor range of 10 cm or more with sensor resolutions in the millimetres range. Much thinner sensor

electrodes used in circuit boards can be used for ranges of up to a few centimetres. Increasing the electrode size results in a corresponding sensor range. Sensors based on capacitance theory can be fitted into integrated circuits or onto printed circuit boards.

2.8 Ice sensors detection

Currently, all the ice detectors available are capable of either one or both of the following:

- Detecting icing event
- Indicating rate of icing

There is no ice detector available that is capable of performing the above-mentioned functions in addition to distinguishing between the two types of in-cloud icing (i.e. glaze ice and rime ice). Distinguishing between rime and glaze ice is important for de-icing power requirement. Depending on the type of ice accreted—glaze versus rime ice—de-icing power requirement will be different. In this research, investigations are performed to investigate and evaluate a new concept for such a sensor or ice detector. As ice sensors can be integrated with ice mitigation systems, it is important for these sensors to relay as much information to the wind turbine controller as to be able to operate anti-icing and de-icing mitigation strategies effectively.

Chapter 3

Theory

3.1 Introduction

This section introduces the working principles of a two-cylinder capacitance ice sensor suitable for placement on a meteorological tower near wind farms or nacelle of a wind turbine. The underlying concept of capacitance and resistance are expanded upon as applicable to the development of the two-cylinder capacitance ice sensor. There is limited literature that details how these concepts can be used for ice detection.

3.2 Working principles of the two-cylinder capacitance ice sensor

The two-cylinder capacitance concept is based on the principle that as ice accretes on two electrically charged parallel-arranged cylindrical probes, the measured capacitance increases while the resistance decreases.

Consider supercooled water drops at ambient temperature, travelling towards the electrically charged cylindrical probes, as shown in Figure 3.1. The likelihood of collision of the supercooled water drops with the cylindrical probes is dependent on both inertia and drag forces acting on the supercooled water drops. If the inertia forces are small compared to the drag forces, the drops tend to follow the air streamlines and go around the cylindrical probes with the air stream (Stokes number <1). The drops deviate from the air streamlines and collide with the cylindrical probes, when inertia forces dominate (Stokes number >1). As the drops collide with the

cylindrical probes and stick on the surface, they freeze and ice begins to grow as shown in Figure 3.2.

The accreted ice affects the electric field generated by the electrically charged cylindrical probes resulting in an increase in capacitance. This increase in the measured capacitance is due to the higher dielectric constant of the accreted ice compared to air. Ice, a dielectric material, in the presence of an electric field becomes polarised, i.e. there is a displacement of charges. The electric field originating from the polarisation charges on the surface of the ice partly shields the external electric field generated by the charged cylindrical probes leading to a reduction in the overall electric field. The overall voltage decreases simultaneously because the electric field is directly proportional to the voltage. Furthermore, assuming a constant charge, the capacitance increases with a decrease in the voltage. Again, the increase in capacitance is due to the presence of ice having a dielectric constant greater than that of the ambient air.

The resistance between the cylindrical probes is large at the start of the icing event because of the air gap between the cylinders. However, as ice builds up on the cylindrical probes, the air gap between the cylindrical probes decreases and the resistance begins to decrease exponentially. The rate of decrease is sensitive to the presence of water on the surface of the iced formed on the cylindrical probes and this phenomenon is used to distinguish between glaze and rime icing.

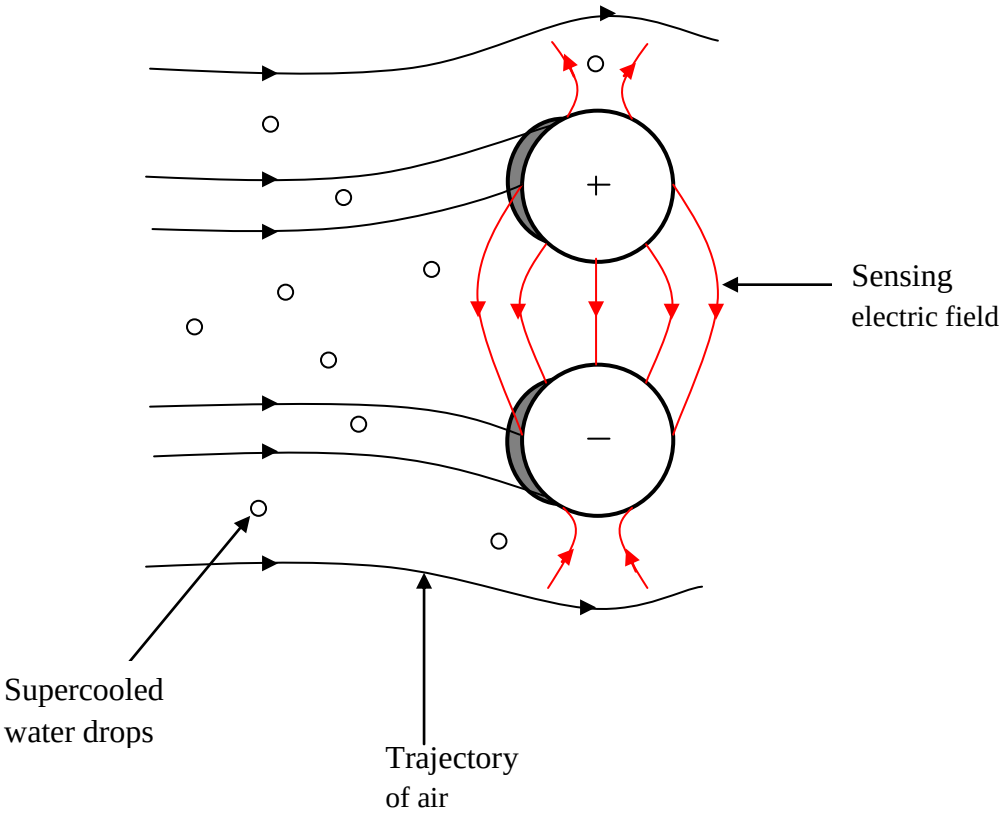

Figure 3.1: Trajectory of supercooled water drops and air moving towards two cylindrical probes

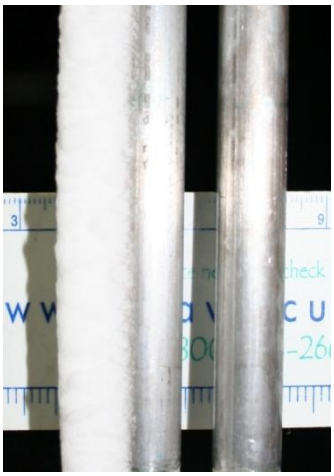

Figure 3.2: Ice formation at the windward side of the cylindrical probes

3.3 Electric field lines

An electric field is generated when two oppositely electrically charged cylinders are brought close to each other as depicted in Figure 3.3. The resulting electric field lines are uniformly distributed, parallel to each other and normal to a small surface on the “inner region” of the cylinders (Figure 3.3).

At locations further from the “inner region”, i.e. along the circumference of the cylinders, the electric field lines are non-uniformly distributed, bulging out (instead of been parallel to each other), as one move away from the “inner region”, as depicted in Figure 3.3. This non-uniformity of the electric field lines in these regions leads to a reduction in the electric field strength. This is known as fringing. A decrease in capacitance is expected with fringing.

The electric field strength is stronger at the “inner region”, weakening along the circumference of the cylinders from the “inner region”. Naturally, for measurement purposes, one would prefer the supercooled liquid water drops to impact, and freeze in the most sensitive regions i.e. in the “inner region”. However, this is not feasible as the aerodynamics of the flow dictates that the ice forms at the windward side (front) of the cylinders.

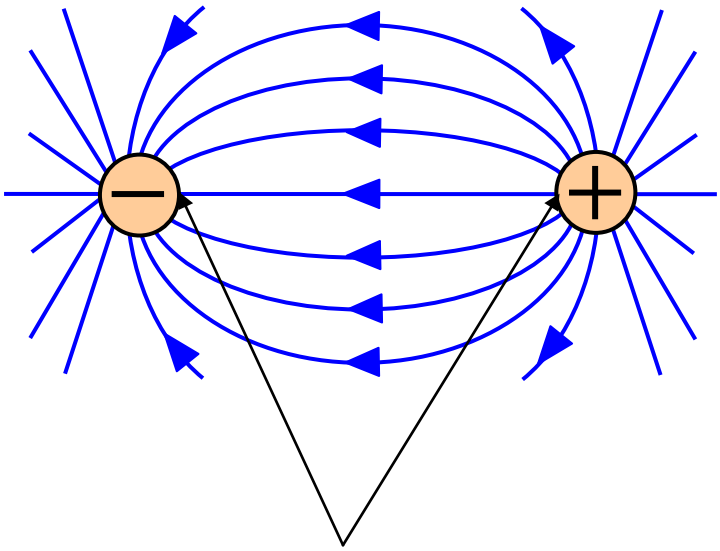

Figure 3.3: Schematic of electric field lines between two opposite charged cylinders

3.3.1 Capacitance between two parallel cylindrical probes

An expression for the capacitance between two cylindrical probes is developed for cylinders of equal diameter, as depicted in Figure 3.4. The following assumptions are made [Kaiser, 2000]:

1. the area around the cylinder is occupied by a vacuum with the implication that the dielectric constant is unity;
2. the cylinders are of infinite length; and
3. the distance between the centers, s, is greater than the diameter, d, of the cylinders.

With the above assumptions, the initial step in developing an expression for the cylinder probes is to set the origin of the coordinate system at the center of the left cylinder.

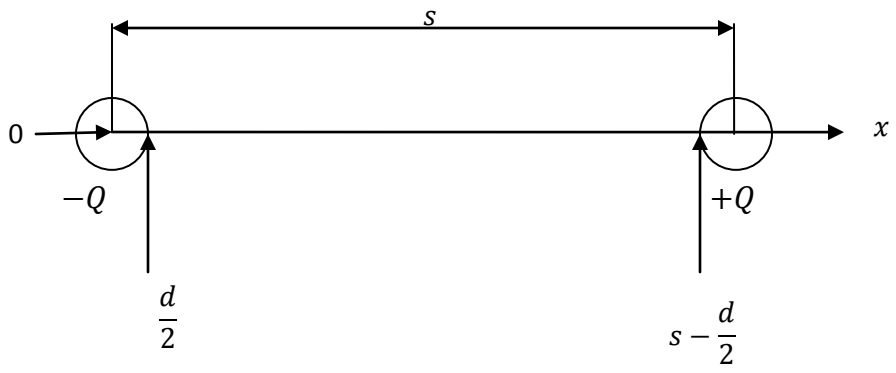

Figure 3.4: Plan view of the two cylindrical probes

The electric field along the line connecting the cylinder centers, created by the left cylinder of charge, $-Q$, is determined assuming the right cylinder is not present. Applying Gauss law, the electric field is given by:

$$E_L = -\frac{Q}{2\pi\varepsilon_o x} \qquad [3.1]$$

where: ε_o is the permittivity of free space which is a constant equal to 8.85 x 10^{-12} *F/m.*

Similarly, the electric field of the right cylinder is given by:

$$E_R = \frac{Q}{2\pi\varepsilon_o (x-s)} = -\frac{Q}{2\pi\varepsilon_o (s-x)} \qquad [3.2]$$

The total electric field is given by the summation of the two fields:

$$E_T = E_R + E_L = -\frac{Q}{2\pi\varepsilon_o}\left(\frac{1}{x} + \frac{1}{s-x}\right) \qquad [3.3]$$

Next, the potential difference, V, between the cylinders is computed by integrating the total electric field along axis, x:

$$V = \int_{\frac{d}{2}}^{s-\frac{d}{2}} E_T dx \qquad [3.4]$$

$$V = -\frac{Q}{2\pi\varepsilon_o}\int_{\frac{d}{2}}^{s-\frac{d}{2}} \left(\frac{1}{x} - \frac{1}{s-x}\right) dx \qquad [3.5]$$

$$V = \frac{Q}{2\pi\varepsilon_o}\left(ln\frac{s-\frac{d}{2}}{\frac{d}{2}} - ln\frac{\frac{d}{2}}{s-\frac{d}{2}} \right) \qquad [3.6]$$

Now, from the third assumption, $s > d$:

$$V = \frac{Q}{2\pi\varepsilon_o}\left(ln\frac{2s}{d} - ln\frac{d}{2s} \right) \qquad [3.7]$$

$$V = \frac{Q}{2\pi\varepsilon_o} ln\frac{4s^2}{d^2} \qquad [3.8]$$

Replacing the diameter, d, with radius r, where $d = 2r$

$$V = \frac{Q}{2\pi\varepsilon_o} ln\frac{s^2}{r^2} \qquad [3.9]$$

$$V = \frac{Q}{\pi\varepsilon_o} ln\frac{s}{r} \qquad [3.10]$$

The capacitance per unit length is given by:

$$\frac{C}{L} = \frac{Q}{V} \approx \frac{\pi\varepsilon_o}{ln\frac{s}{r}} \qquad [3.11]$$

The computed capacitance has units of *F/m*. Equation 3.11 indicates that, the capacitance depends on the distance between the cylinders (decreasing with increasing s).

If the space around the cylinder is now filled with a dielectric, which is an insulating material, the measured capacitance increases by a dimensionless factor ε_r, which is the dielectric constant of the introduced material. Equation 3.11 then becomes [Kaiser, 2000]:

$$\frac{C}{L} \approx \frac{\pi\varepsilon_o\varepsilon_r}{ln\frac{s}{r}} \qquad [3.12]$$

In general, when a dielectric electric material is placed in the proximity of an electric field, there is a redistribution of charges within its atoms or molecules. This happens because of the polarisation of the dielectric material, producing charge concentrations on its surfaces that create an electric field opposed to that of the capacitor. Since an electric field is a vector quantity, the resultant electric field is weaker. As the electric field weakens, the voltage and the capacitance increase.

The dielectric material occupying the gap between the cylindrical probes in some instances can be made of more than one material, and since the calculated capacitance is dependent on the dielectric constant, the various dielectric constants need to be taken into account. The first step in the determination of effective capacitance for a compound material is to have afore knowledge of

how the dielectric materials are spatially arranged, i.e. either series or parallel or both. With this information, series or parallel capacitance theory can be used to compute the effective capacitance [Ahmed and Ismail, 2008]. This technique assumes that the electric field is shielded, i.e. confined entirely between the cylinders without any fringing field. This technique is applicable to porous dielectric materials as well. For simple arrangements, the accuracy of this technique is excellent. However, for complex arrangement such as ice with ice pockets, it is not easy to compute the effective capacitance, which could make developing a theoretical expression for rime ice more difficult.

In summary, the presence of a dielectric material increases the measured capacitance and because the dielectric constants are generally a unique material property, it is possible to detect the presence of a material using changes in measured capacitance as described above.

3.3.2 Resistance between two parallel-arranged cylinders

The electrical resistance of a material gives a measure of how it opposes the flow of an electric current. The resistance of a resistive material is related to the potential difference (V) and current (I) by Ohm's law [Paul, 2000].The resistance of a uniform material is a function of the length (L), cross sectional area (A) and the resistivity of the material (ρ) [Paul, 2000].

Generally, insulators offer high degrees of opposition to the flow of electric currents. Air is an excellent insulator. Consider the two cylinders configuration in Figure 3.1, with an air gap between them. If a potential difference is applied across the cylinders, the measured electrical resistance can be assumed to be infinite since the circuit is open circuit or severed due to the presence of the air gap. Now, as the two cylinders are brought closer to each other, there is a

reduction in the air gap, with the measured electrical resistance approaching a small value as they begin to touch. Therefore, reduction in the air gap forward of the probe resulting from ice accretion will lead to a similar reduction in the measured resistance. Additionally, since the electric field will interact with the surface of the iced region, conditions pertaining will aid in distinguishing between the ice types based on resistance.

Chapter 4

Experimental and numerical procedures

4.1 Introduction

An experimental and theoretical program was designed to evaluate a new concept for the detection of ice, estimation of ice accretion and to distinguish between rime and glace ice based on the measurement of capacitance and resistance change between two electrically charged cylinders as ice accretes on the cylinders. For ease of discussion, the cylindrical probes with ancillary equipment were defined as the ice sensor. The ice sensor is described in detail in Section 4.2. Section 4.3 describes two-dimensional numerical simulations used to solve the electric field equations to determine the optimal center-to-center distance between the cylindrical probes and understand the variation of capacitance with ice deposition and growth of ice. These numerical simulations were validated with a series of laboratory experiments described in Section 4.4. Finally, Section 4.5 deals with the experiments performed in the icing wind tunnel to test the sensitivity and reproducibility of the ice sensor under various icing conditions. These experiments were performed in the University of Manitoba Icing Wind Tunnel Facility.

4.2 Description of the two-cylinder capacitance ice sensor

The ice sensor consisting of two cylindrical probes made of aluminum connected to a capacitance meter and computer to collect data are shown in Figure 4.1. Aluminum was selected for its machinability, high corrosion resistance and relatively low cost. The two cylindrical probes were made to have equal lengths to eliminate non-uniformity in the sensing electric field [Elkow and Rezkallah, 1996]. The length and the diameter of the two cylindrical probes were

selected to minimise three-dimensional effects. An insulator of height 3 cm was fitted at the base of the probes. This was done to prevent spikes in capacitance due to accumulation of water and ice that deposit due to gravity at the base. The insulator was required to be non-conductive, machinable and of low cost. Based on these criteria, Ultra High Molecular Weight (UHMW) polyethylene was selected. The polyethylene was pressed fit to the aluminum electrodes. The cylindrical probes were connected to a Hioki 3522-50 capacitance meter by lead wires. These lead wires were selected to minimize parasitic capacitance. The Hioki 3522-50 capacitance meter is an impedance meter with improved power for high-speed measurements of 5 ms and with an accuracy of ± 0.08%. Data was collected at 100 KHz. The meter was connected to a computer via an RS232 cable for data storage [Hioki, 3522-50 LCR HiTESTER, 2007].

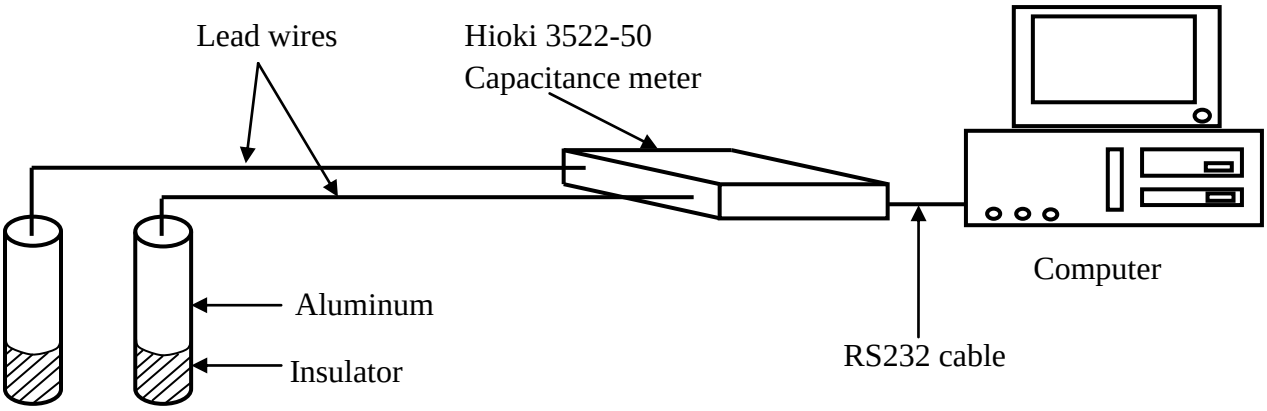

Figure 4.1: Schematic two-cylinder capacitance sensor and ancillary equipments

4.3 Numerical simulations

This section introduces the set of numerical experiments performed using Quickfield™ electric field professional software. The aim of these experiments was in part to the determine the

optimal design dimensions for the cylindrical probes. Quickfield™ solves the two-dimensional Poisson's governing equations using the Domain Decomposition Method finite element technique [QuickField™, 2005].

The various cases considered in the numerical experiments are shown in Figure 4.2. In the first case study, different center-to-center distances, *s*, were considered using air as the dielectric material surrounding the cylindrical probes (Figure 4.2a) to determine the optimal center-to-center distance (*s*) between the cylindrical probes. Additionally, the electric field distribution predicted by QuickField™ was used to characterise regions of high electric field strength (high sensitivity) to ice deposition. In the second case, the effect of decreasing the diameter of one of the cylindrical probes on the ice sensor's sensitivity was studied (Figure 4.2b). In this case study, D is the varying diameter while d is the fixed diameter, 1.27 cm. For the third case, ice depositions of varying thickness, *t*, were modelled around the cylindrical probes at both the front (i.e. parallel orientation of probes) and side (i.e. inline orientation of probes) iced regions to investigate the dependence of the ice sensor's sensitivity on the location of accreted ice (Figure 4.2c and 4.2d). In these experiments, the dielectric material comprise of both air and ice. In the fourth case, ice depositions of varying thickness were modelled around the cylindrical probes to investigate the variation of ice growth with capacitance (Figure 4.2e).

4.3.1 Numerical procedure

As discussed earlier, Quickfield™ solves the two-dimensional Poisson's governing field equations using the finite element method. The charged cylindrical probes were modelled as two-dimensional equipotential circular surfaces. A non-uniform mesh was use: a dense mesh defined around the cylindrical probes and a more course mesh far from the cylindrical probes. The

external domain was assigned a zero potential. The areas within the computational domain were assigned the appropriate dielectric constants. For the special cases where the optimal center-to-center distance, s, was determined and the effect of reducing the diameter of one of the electrodes was investigated, the domain is assigned a dielectric constant of air. For ice, an estimate of 3.1 was used for the dielectric constant and 1 for air. Three different mesh densities and boundary sizes were considered for grid and domain independence respectively.

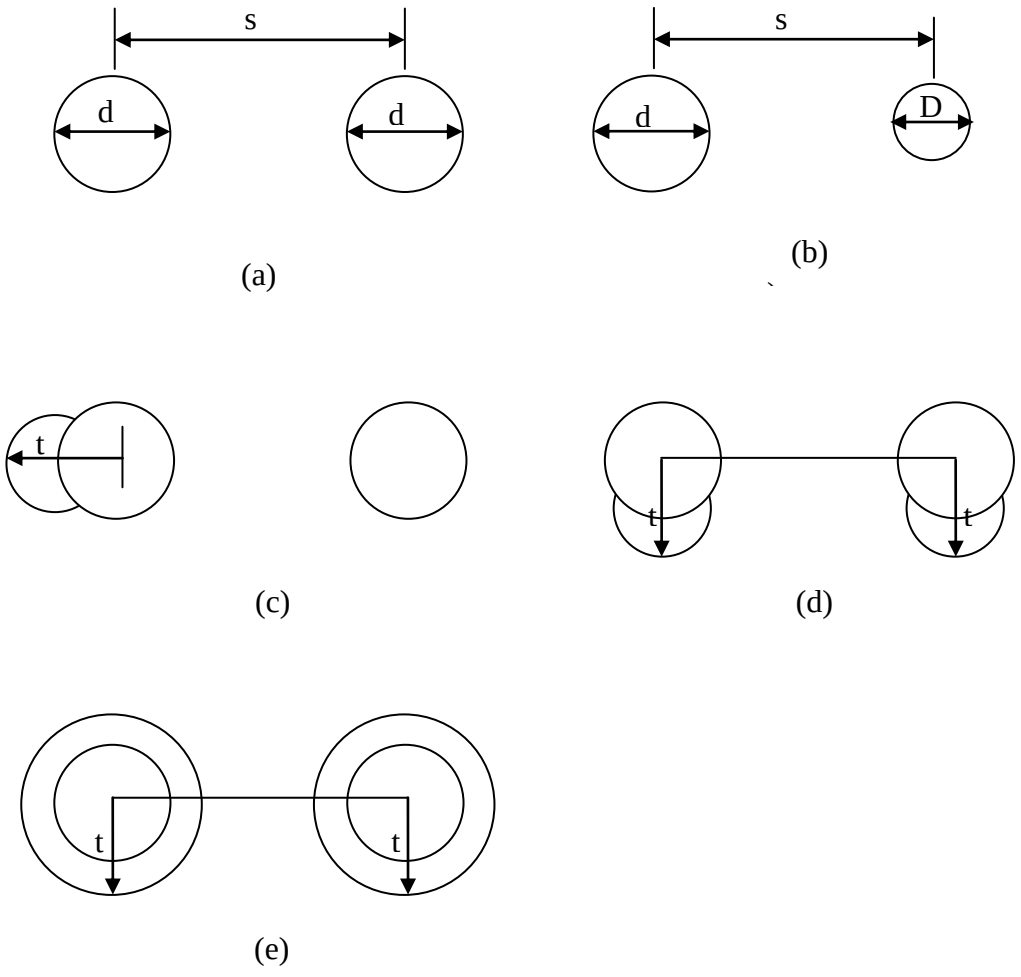

Figure 4.2: Cases considered for numerical simulation

It was found that even though 100,000 mesh nodes was required to obtain grid independence with 1% error compared to the theoretical results for two parallel cylinders (Equation 3.12), 500,000 mesh nodes were used in subsequent studies since the computationally time between the two were of the order of a few seconds. For domain independence, a size of 38 times the diameter of the cylindrical probe was sufficient for results to vary less than 2% but 40 times the diameter of the cylindrical probe was selected. Figure 4.3 shows a typical computational domain that is used to solve the field equations.

4.4 Acrylic sleeve experiment

Before the ice sensor was tested in the wind tunnel, a series of tests were designed and performed to understand the variation of capacitance with a "modelled" ice growth in a laboratory setting possessing an exact geometry to validate the numerical experiments. The "modelled" ice of precise geometry and uniform density was simulated using a material that has a dielectric constant similar to that of ice. Acrylic was selected and was precisely machined into pairs of hollow cylindrical sleeves with the same height but varying outer diameters. The varying outer diameters were designed to depict varying thickness of ice. Another set of acrylic sleeves with holes from the inner radius to outer radius around the circumference of the sleeves was also machined. The rationale behind the use of acrylic sleeves with holes was to investigate the effect of air pockets on the measured capacitance during rime ice formation. The components of the experimental set up are shown in Figure 4.4.

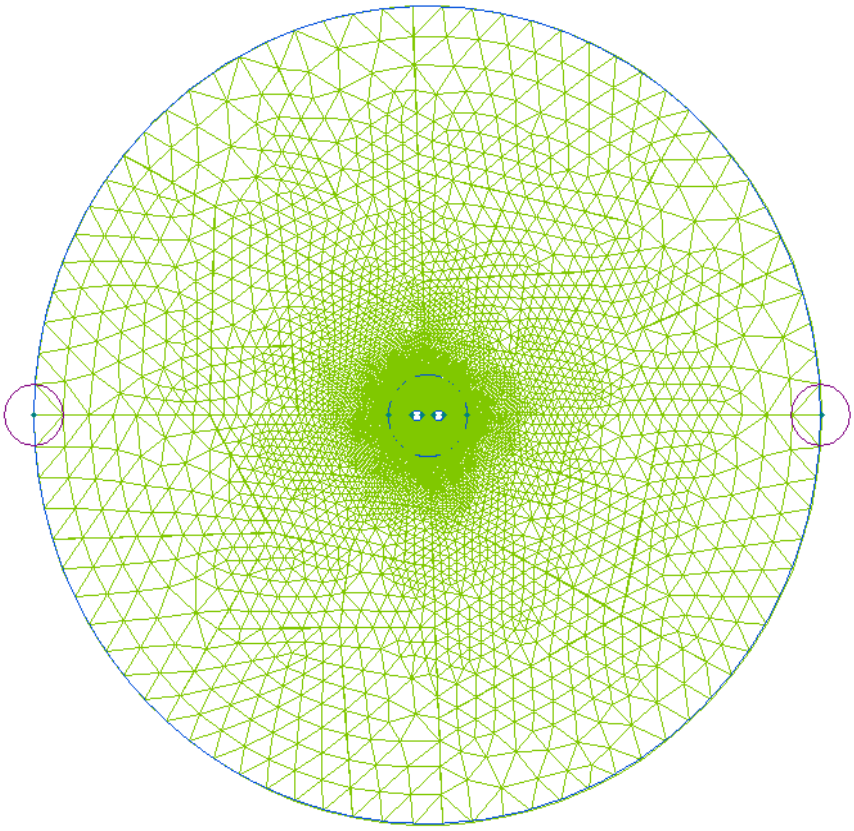

Figure 4.3: 500,000 node computational domain

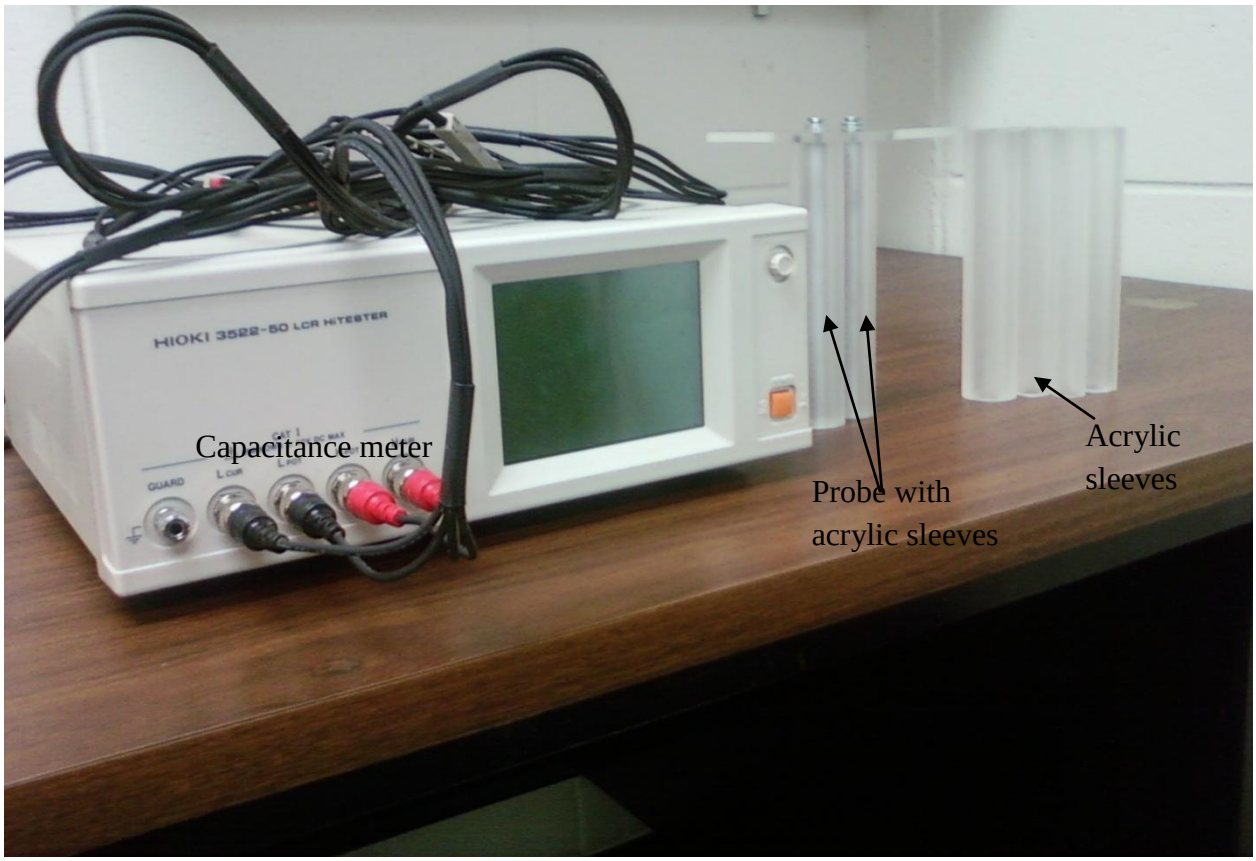

Figure 4.4: Components of model icing experimental set up

4.4.1 Acrylic experiment procedure

With the cylindrical probes secured in the supporting base, the capacitance meter was allowed to stand for an hour to warm up. Afterwards, a single or pair of acrylic sleeves of the same size was then slipped around one or two of the cylindrical probes. The capacitance meter was then connected to the cylindrical probes via the lead wires. The setup was allowed to stand for five minutes for the readings to stabilize, before the measured capacitance was recorded. The lead wires were disconnected from the cylindrical probes, the pair of acrylic sleeves slipped off and the next pair of acrylic sleeves slipped back onto the cylindrical probes. The procedure was then repeated. These set of experiments were generally performed three times to test reproducibility.

The experimental procedure was repeated for the following cases:

- single acrylic sleeve on one of the cylindrical probes; and
- pair of acrylic sleeves of the same size and height with holes from inner radius to outer radius around the circumference slipped onto both cylindrical probes.

The dimensions of the acrylic sleeves are summarised in Table 4.1 and Table 4.2. Results of these tests are presented in Chapter 5.

Table 4.1: Dimensions of acrylic sleeves

Outer diameter (cm)	**Center-to center (cm)**	**Length of cylindrical probes (cm)**
1.27	2.8	15
1.37		
1.47		
1.67		

Table 4.2: Dimensions of porous acrylic sleeves

Diameter of holes drilled around the circumference of the sleeves (cm)	**Outer diameter of porous sleeves (cm)**	**Number of holes around the circumference**
0.15	1.87	464
0.20		
0.15	1.77	
0.20		

4.5 The University of Manitoba icing wind tunnel

4.5.1 The icing wind tunnel

The ice sensor was tested under simulated icing conditions in the Icing Wind Tunnel Facility located in the Engineering Building of the University of Manitoba. This facility is a closed loop refrigerated wind tunnel capable of producing wind speeds up to approximately 32 m/s over a rectangular test section. In this facility, air temperatures as low as -40°C can be achieved. A spray bar system located upstream of the test section produces the icing cloud with the drops sizes in the range of 10 μm to 1000 μm (Median Volume Diameter of 100 μm) [Wang, 2008]. The spray bar has four nozzles in a streamline shell made of aluminum. The nozzles are

uniformly spaced to facilitate uniform distribution of the spray drop. Heating strips are installed between nozzles and the aluminum shell to prevent the nozzles from clogging during low temperature experiments. The distance from the spray bar to the test specimen is sufficient for the drop to equilibrate with the ambient temperature before impact with the test specimen and transforming into ice. Although the spray drops fills the entire test section, a central region of constant liquid water content exist where the test specimen are located for each test. The liquid water content can be varied from 0 to 2 g/m^3 [Wang, 2008]. The ambient air velocity is adjusted by varying the frequency of the fan blower motor. The window of the cold chamber is heated in order to keep the surface free of frost and allow for visibility. For easy access to the spray bar, test specimen adjustment, cleaning after a test and for maintenance purposes, doors are provided at vantage points along the perimeter of the tunnel. Figure 4.5 is a photograph of the inner duct of the icing wind tunnel.

4.5.2 Icing wind tunnel calibration

Kraj [2007] previously did the calibration of the icing wind tunnel. The aim of the calibration was to test the conditions for which glaze and rime ice can be simulated successfully. To calibrate the tunnel, a series of tests were performed at varying temperatures to obtain data on wind speeds in the inner duct of the icing wind tunnel. To do this, a pitot-tube manometer was mounted behind the spray nozzles i.e. upstream of the inner duct of the wind tunnel while a three-cup anemometer was placed downstream of the spray nozzles. The purpose of these devices were to check the accuracy in the frequency of the wind tunnel motor fan and to calibrate it for producing the correct wind speeds at these given temperatures. For detailed results on this calibration, see Kraj [2007].

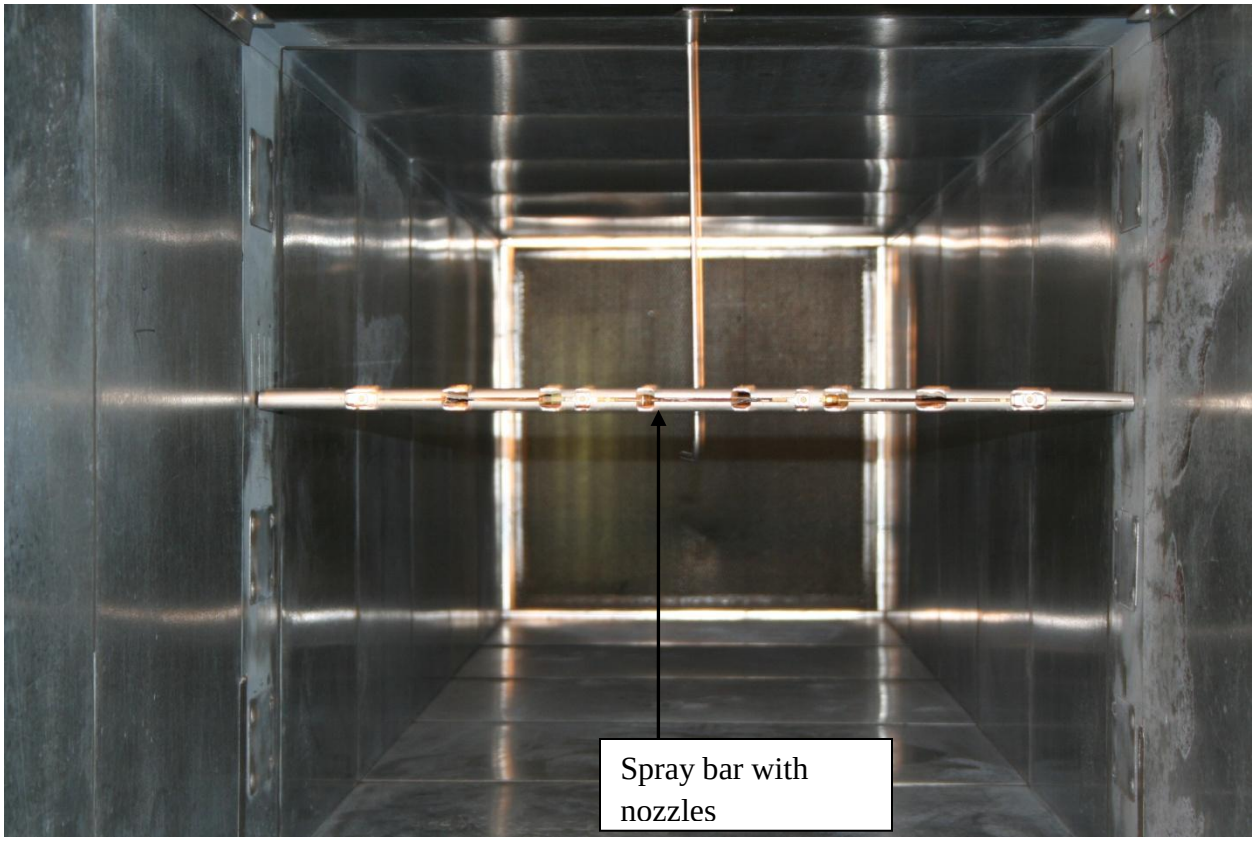

Figure 4.5: Wind Icing Tunnel

4.5.3 Experimental conditions

Rime and glaze ice were the two icing events simulated in the icing wind tunnel when the ice sensor was tested. Rime ice forms at lower temperatures under low liquid water content while glaze on the other hand forms at temperatures near the freezing point under high liquid water content. To simulate these two distinct icing events in the wind tunnel; temperature, flow rate (which regulates the liquid water content) and the wind speed must be set appropriately. A summary of the experimental conditions are shown in Table 4.3. The temperature values were selected taking into account the error margin in the accuracy of the icing wind tunnel

thermocouples. The liquid water content (LWC) was estimated from rime ice growth. See Appendix A for details.

Two orientations in relation to the wind and supercooled water drops direction were performed for all icing conditions. The inline orientation has one cylindrical probe facing the impinging supercooled water drops while the parallel orientation has both cylindrical probes facing the impinging supercooled water drops. The schematic of these orientations is shown in Figure 4.6.

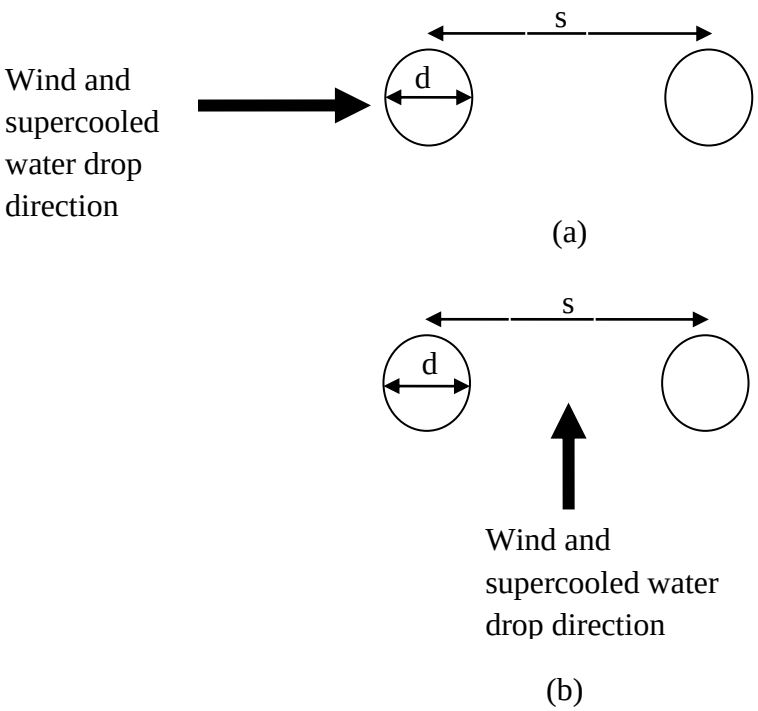

Figure 4.6: Schematic of (a) Inline and (b) Parallel orientations of the cylindrical probes in relation to the wind and water drop direction

4.5.4 Experimental procedure

The spray nozzles were first calibrated to deliver uniform flow by adjustment of individual valves on each nozzle water lines. With the water spray system turned off, the cylindrical probes

were mounted on a support bar that spanned the length of the inner duct of the icing wind tunnel. The location of the cylindrical probes on the bar was selected to be away from the walls of the inner duct to have a homogenous ice growth and to eliminate the boundary layer effects. The lead wires were connected to the cylindrical probes and back to the capacitance meter located outside the tunnel. The capacitance meter was allowed to stand for an hour to warm up before the start of the experiment. The tunnel air temperature was set to the required value for the formation of a particular type of ice required. When this temperature was reached and stabilised, the spray system was activated. The spray bar water mass flow rate and the injection pressures set the required liquid water content and median volume diameter. Experiments were performed at 3, 4, 5, 10 and 20 minutes at each icing condition, wind velocity and orientation of cylindrical probes. Capacitance and resistance was recorded every 5 seconds. Photographs were taken after the experiments, and mass and thickness of the ice were measured. Mass and thickness were measured as follows. The wind icing tunnel was turned off while ensuring the inside conditions stays constant. The thickness of the ice was measured with a vernier calliper at various locations and averaged. The accreted ice is then scrapped of the cylindrical probe(s) into a beaker and weighed. Three icing experiments for both rime and glaze ice were performed to test the reproducibility of the results. Results of these tests are presented in Chapter 5.

Table 4.3: Experimental conditions for wind icing tunnel tests

Temperature (^{o}C)	**Type of icing event**	**Liquid water content, LWC, (g/m^3)**	**Ambient velocity (m/s)**	**Sensor orientation to ambient air**
-2 (±2)	Glaze	2.0	5 (±1) 8 (± 1) 10 (± 1)	Inline Parallel
-10 (±2)	Rime	0.8	5 (±1) 8 (± 1) 10 (±1)	Inline Parallel

4.6 Error in measurements

Measurement errors in the measured thickness, mass and capacitance were determined as follows. To estimate the measurement errors in the mass and thickness of, three repeated measurements were performed at time intervals of 3, 5, 10, 15 and 20 minutes under both rime and glaze ice conditions for the parallel probe orientation and a single wind speed of 5m/s. Afterwards, the standard errors of the measurements were calculated. It was assumed this error is similar for the other wind speeds and the inline orientation. The results are shown in Figure 4.7. The standard errors calculated for the measured mass of rime ice accreted ranges from 0 to 0.12 g while for glaze ice; it ranges from 0 to 0.76 g as shown in Figure 4.7. Generally, the standard errors computed for glaze ice were greater than rime ice for both mass and thickness. These

relatively higher computed standard errors in mass for glaze ice can be attributed to predominantly the difficulty in removing all the accreted ice from the cylindrical probes for measurement after the experiments, and to a lesser extent, the time delays in activating and deactivating the spray bar systems during experimentations. The computed standard error for the measurement for both rime and glaze ice ranged from 0 to 0.11 mm and 0 to 0.87 mm, respectively as shown in Figure 4.8. The relatively higher standard error for glaze ice was due to the horns on the surface which made the thickness measurement difficult.

The current sensor is sensitive to any change in the position of the lead wires connecting the two cylindrical probes since it contributes significantly to parasitic capacitance. Additionally, it is also sensitive to the ambient conditions. To estimate the measurement errors, three repeated experiments were performed. The capacitance variation with time and sizes of acrylic recorded for wind icing tests and for acrylic tests were measured. The results are shown in Figure 4.8 and Figure 4.9 for icing wind experiments and acrylic experiments, respectively. The standard error estimates for glaze ice experiments ranges from 0 to 0.27 pF while for rime ice it ranges from 0 to 0.21 pF. The variations in the ambient conditions within the icing tunnel can be attributed to the standard errors computed. For the acrylic experiments, the ability to maintain near constant ambient conditions during experimentations resulted in relatively lower computed standard errors.

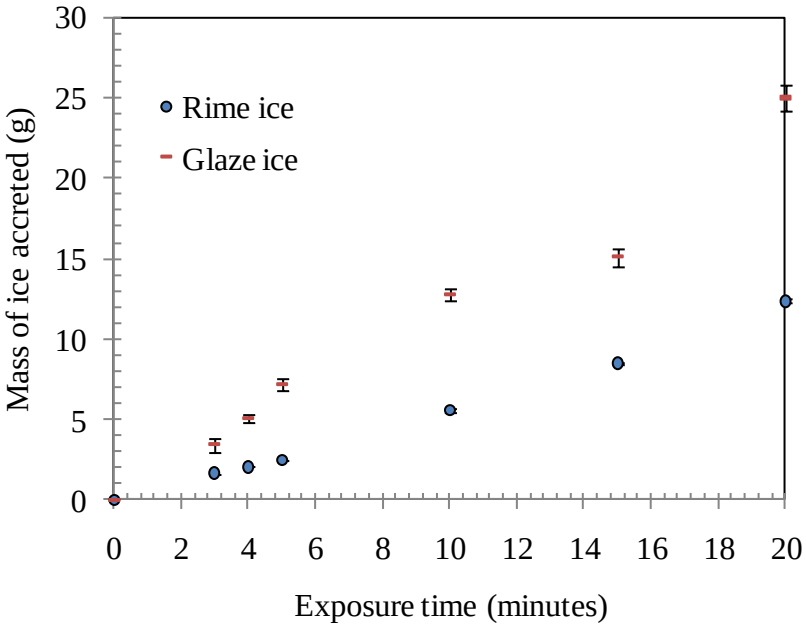

(a)

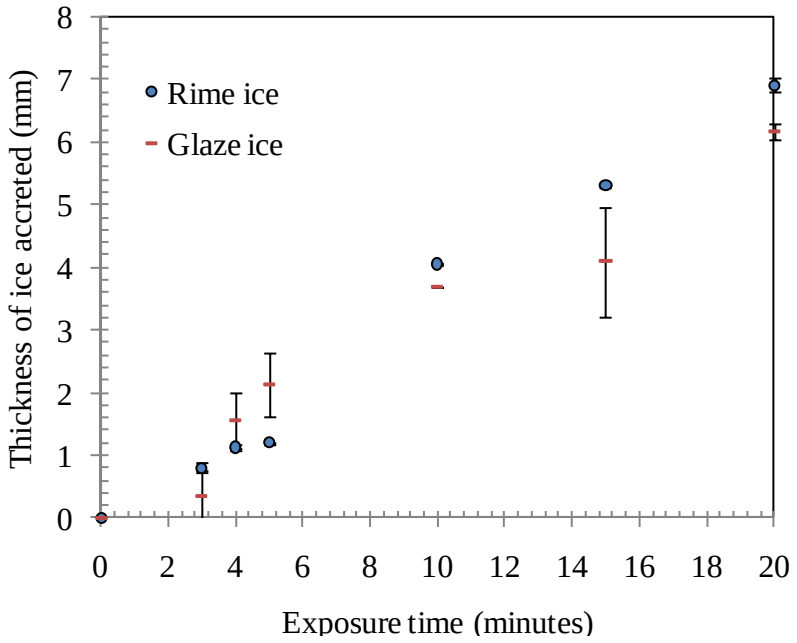

(b)

Figure 4.7: Standard error estimates in the measured (a) mass and (b) thickness for both rime and glaze ice at wind velocity of 5 m/s for parallel probe orientation

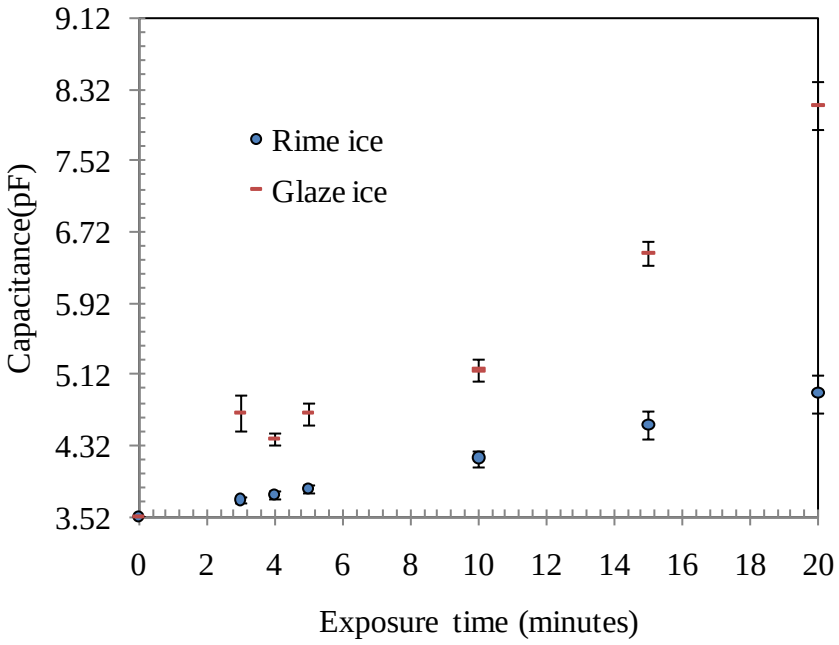

Figure 4.8: Standard error estimates in the measured capacitance for both rime and glaze ice at wind velocity of 5 m/s for parallel probe orientation

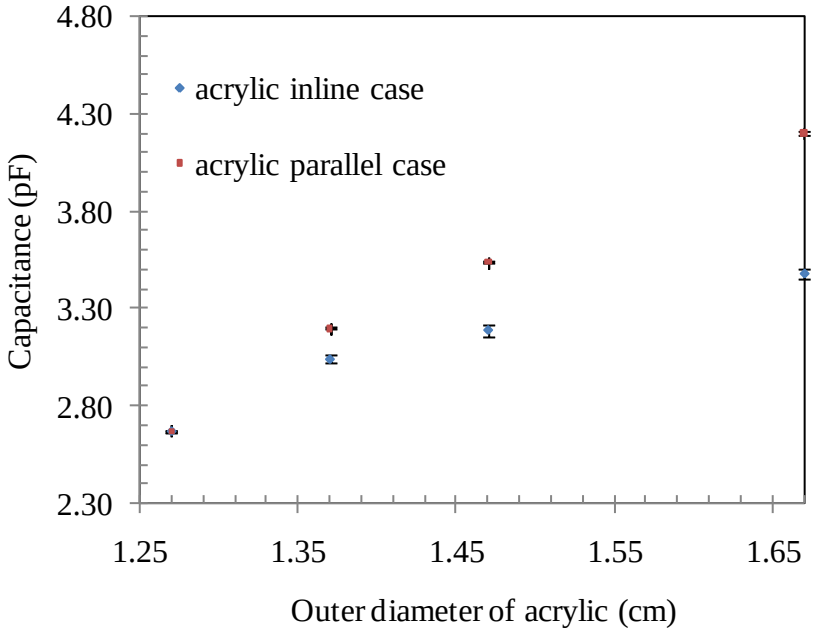

Figure 4.9: Standard error estimates in the measured capacitance for acrylic experiments

Chapter 5

Results and Discussions

5.1 Introduction

This chapter presents and discusses the numerical and experimental results. The numerical and acrylic results are discussed in Section 5.1. In Section 5.2, the wind icing tunnel experiments results are presented and discussed. Finally, the optimal sensor configuration is presented in Section 5.3.

5.2 Numerical and acrylic studies

The capacitance based numerical study indicates that the sensitivity of this sensor increases approximately at an exponential rate as the center-to-center distance, s, of the cylindrical probes decreases (Figure 5.1). This result is consistent with well-established analytic solutions, and is due to the increase in the strength of the electric field as the distance between the centers of the cylindrical probes decrease. However, in the present application there is a limit to how short the center-to-center distance can be selected, since bringing the probes too close to each other will lead to early bridging of ice between the probes. Early bridging is a local effect that does not span cylinders and can result in over prediction of the icing rate. Additionally, results from early bridging can be misleading, especially since the time to deice needs to be inferred from sensor measurements. Based on both the results in Figure 5.1 and the concerns for early bridging, a center-to-center distance of 1.87 cm was selected.

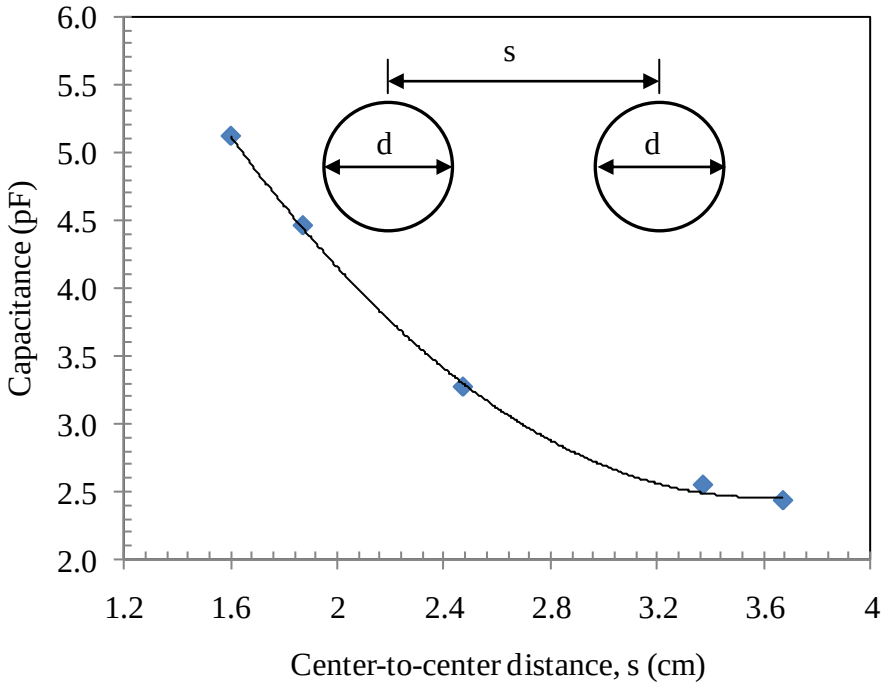

Figure 5.1: Capacitance variation with probe centre-to-centre distance, s

The predicted electric field distribution for s = 1.87 cm, shown in Figure 5.2, was used to investigate regions of high sensitivity to ice accretion. This was done by considering the distribution of the electric field lines around the cylindrical probes. Where the electric field lines are farther apart, the electric field strength is weaker than where they are closer together. The electric field lines are more concentrated between the cylindrical probes, becoming weakly distributed towards the front and side surfaces of the cylindrical probes. It is apparent that the ideal location for ice deposition would be between the cylindrical probes where the electric field lines are denser, i.e., greater electric field strength.

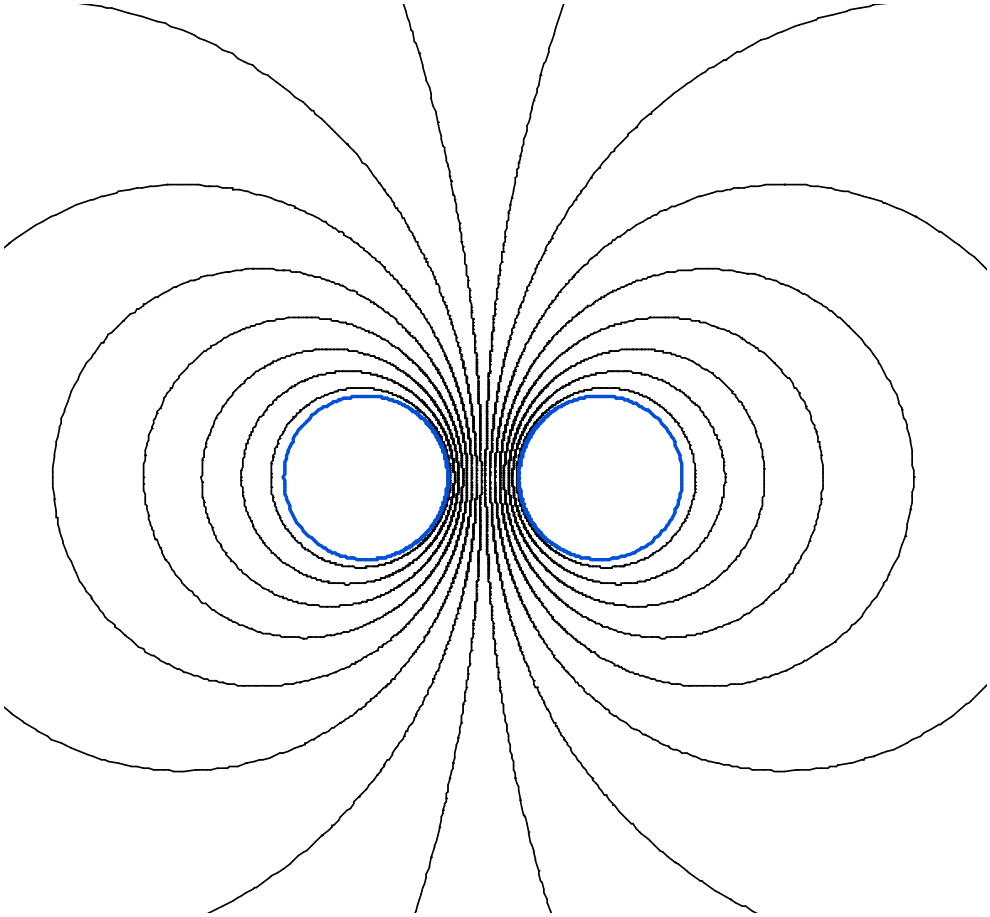

Figure 5.2: Electric field distribution calculated using QuickField™, s = 1.87 cm, d = 1.27 cm, Q = 1 C

Based on the above observation, the case of two cylindrical probes with one smaller than the other was investigated as a potentially more sensitive geometry to ice accretion. The concept was to increase ice accretion between the probes, i.e. region most sensitive to ice accretion, by orienting the probes inline with the flow direction with the smaller probe in the upstream position. In this orientation, the stream of supercooled water drops flow past the smaller probe and impinges on the front surface of the larger probe. There were however two major drawbacks

to this concept. Firstly, results from QuickField™ simulations indicate a reduction in the sensitivity of the sensor with a reduction in size of one of the cylindrical probes, as shown in Figure 5.3. Secondly, numerical studies of flow around two unequal cylindrical probes using Fluent™ indicates that, to achieve a high deposition rate of supercooled drops on the larger downstream probe, a long center-to-center distance between the probes is required for drops that flow past the smaller upstream probe to move towards the front of the downstream probe. As discussed above, this would inevitably lead to a reduction in the sensitivity of the probe. A decrease of 18% was observed when the diameter of one of the electrodes was reduced from 1.27 cm to 0.89 cm for s=1.87 cm. Therefore, only probes of equal diameter were considered for further study.

The sensitivity of the sensor as a function of the orientation of the two-cylindrical probes to the supercooled water drops was investigated numerically using QuickField™. This was done by modelling ice of varying thickness around the front surface of the two-cylindrical probes for the case of parallel orientation while for the inline case; ice was modelled on the side surface of one of the probes (see Figure 4.2c and Figure 4.2d). It should be noted that since QuickField™ is a two-dimensional software package, more complex geometries of ice observed during icing experiments cannot be modelled accurately. Hence, simple geometries of ice with varying thickness were modelled and the variation of capacitance with probe orientation studied. The results from the simulations, shown in Figure 5.4, indicate an increase in capacitance as the thickness of the modelled ice increases. Additionally, the capacitance values for the parallel orientation case were found to be higher than the inline orientation case. This indicates a higher sensitivity for the parallel orientation compared to the inline orientation. This is due to the denser

distribution of electric field lines in front of the probes compared to the sides as shown in Figure 5.2 and the larger amount of modelled ice in front of the parallel oriented probes.

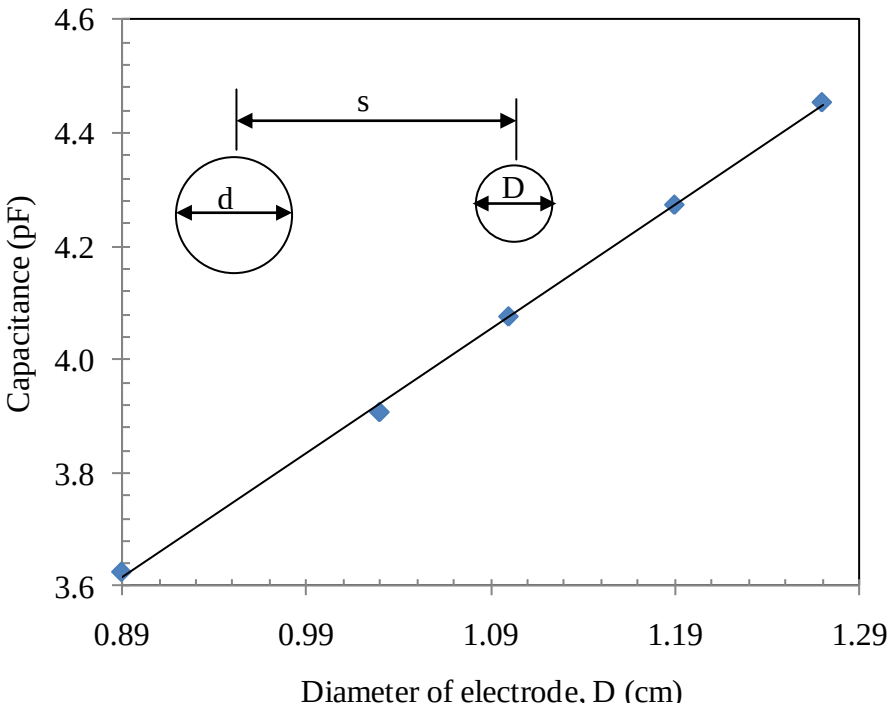

Figure 5.3: Effect of decreasing the diameter of one of the cylindrical probes on the capacitance; larger probe diameter, d=1.27 cm and s=1.87 cm

The acrylic experiments, which were designed to validate the numerical experiments, also indicated an increase in capacitance with an increase in the size of the acrylic sleeve. The results as shown in Figure 5.5 indicates that the measured capacitance with a single sleeve on one of the cylindrical probes was smaller compared to an acrylic sleeve on both cylinders. In these experiments, a single sleeve slipped around one of the cylindrical probes depicts the case where the probe is oriented inline, while the case where both cylindrical probes have acrylic sleeves around them depicts the parallel orientation. The results affirm the results from the numerical

simulations (see Figure 5.4) that the parallel orientation is the more sensitive of the two orientations. The capacitance values from field calculations were smaller compared to the acrylic results. Initially, the dielectric constant was believed to be the cause of this discrepancy. However, the results were still smaller compared to the acrylic results after various dielectric constants (within the range for acrylic) were assumed. Other possible causes of this discrepancy include the capacitances in the lead wires and two-dimensional effects. The trend of an increase in the measured capacitance with increasing size of the acrylic sleeves are in agreement with results from QuickField™, as shown in Figure 5.5.

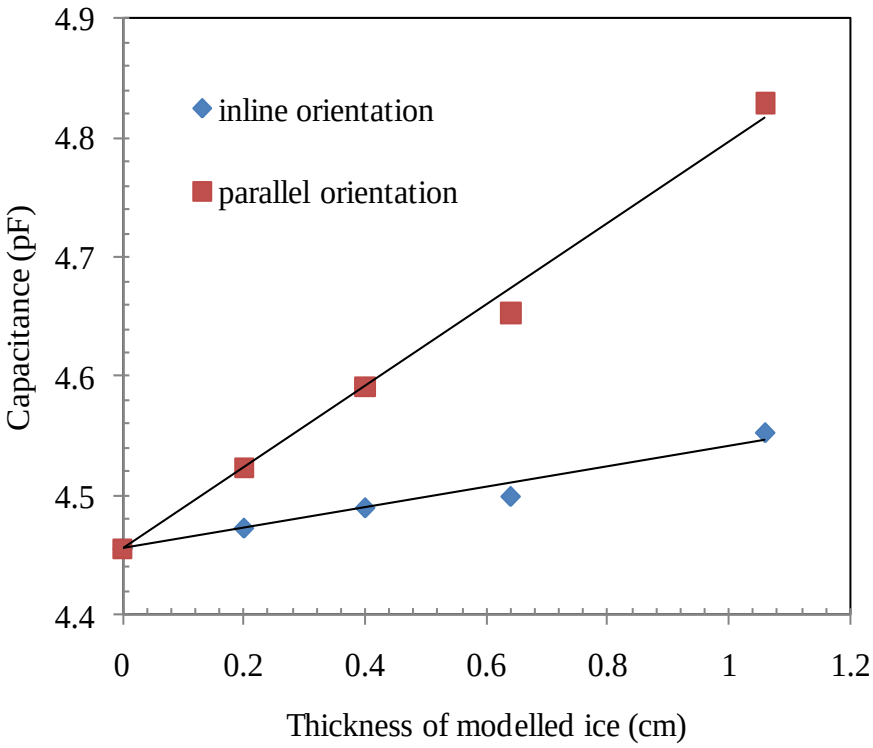

Figure 5.4: Sensitivity of ice accretion to probe orientation

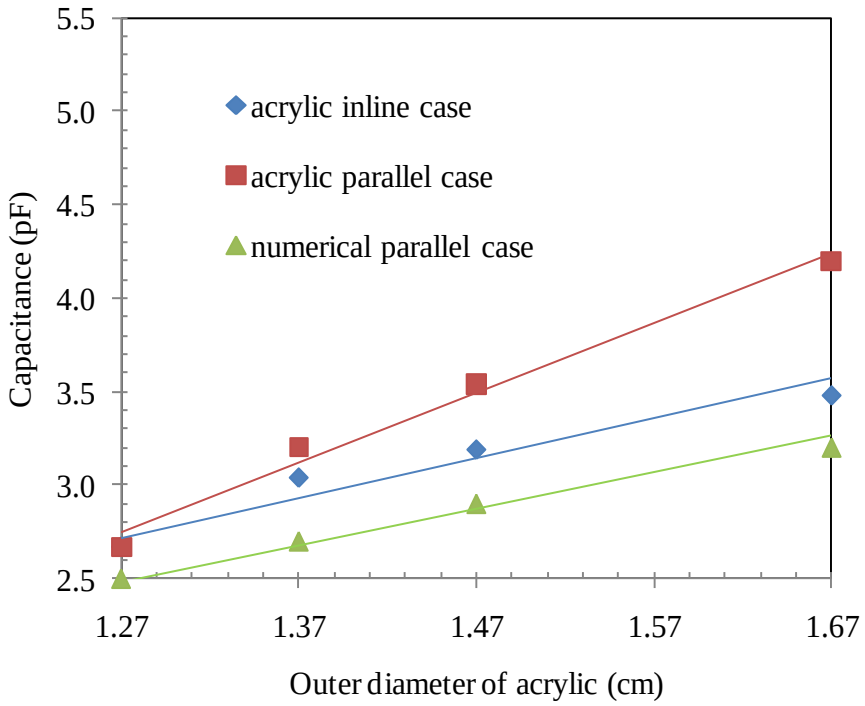

Figure 5.5: Capacitance variation with size of acrylic sleeves. Inline case has a single sleeve on one of the cylindrical probes while parallel case has sleeves on the two cylindrical probes

A summary of the porous acrylic sleeves experiment results are shown in Table 5.1. This experiment was performed to investigate the effect of air pockets in ice structures on the measured capacitance, important for rime ice. The results indicate a decrease in the capacitance as the size of the holes drilled along the circumference of the acrylic sleeves increase. An increase in size of the holes corresponds to an increase in the ratio of air to acrylic. With all other factors remaining constant, the capacitance will depend on the volume of the drilled holes. The volume of the large drilled holes is greater than the volume of the small drilled holes. The implication of this will be a higher ratio of air to acrylic in favour of the larger drilled holes. Since the capacitance of air is less than acrylic, a large drilled hole will have a smaller capacitance compared to a smaller hole.

Table 5.1: Summary of porous acrylic sleeves experiments

Diameter of holes drilled around the circumference of the sleeves (cm)	**Pitch**	**Outer diameter of acrylic sleeves (cm)**	**Capacitance measured (pF)**
0.15	0.3	1.87	3.27
0.20			3.19
0.15		1.77	3.12
0.20			3.05

5.3 Wind icing tunnel experiments

5.3.1 Experiments at -10^{o}C

Rime ice was simulated at -10^{o}C under low liquid content conditions and the resulting ice accretion is shown in Figures 5.6 to 5.8. All impinging water drops froze (accretion efficiency = 1) upon impact on the cylindrical probes for both the inline and parallel orientations. Minimal spreading or flatting was observed and air spaces were incorporated into the resulting ice structure. The general appearance of the ice formed was white and opaque for both orientations. The middle surface of the accreted ice on the cylindrical probes was relatively smooth with feather-like features on the edges. This feathered structure became more pronounced as shown in Figure 5.6 for times of 4 and 15 minutes, respectively. Initially, the ice growth was from the center of the front face to the sides of the cylindrical probes for both inline and parallel orientations, as shown in Figures 5.7 and 5.8. This initial growth direction changed after approximately 5 minutes, and started to grow outward only, relative to the free stream air direction. The cross-sectional shape from the top view of the accreted ice was convex with the radius of curvature increasing with time. Along the length of the probes, profiles of the accreted ice were uniform during the first few minutes of the experiments. In time however, the ice profiles became non-uniform along the length of the probes due to changes in the aerodynamics of the flow leading to variations in local collision efficiency.

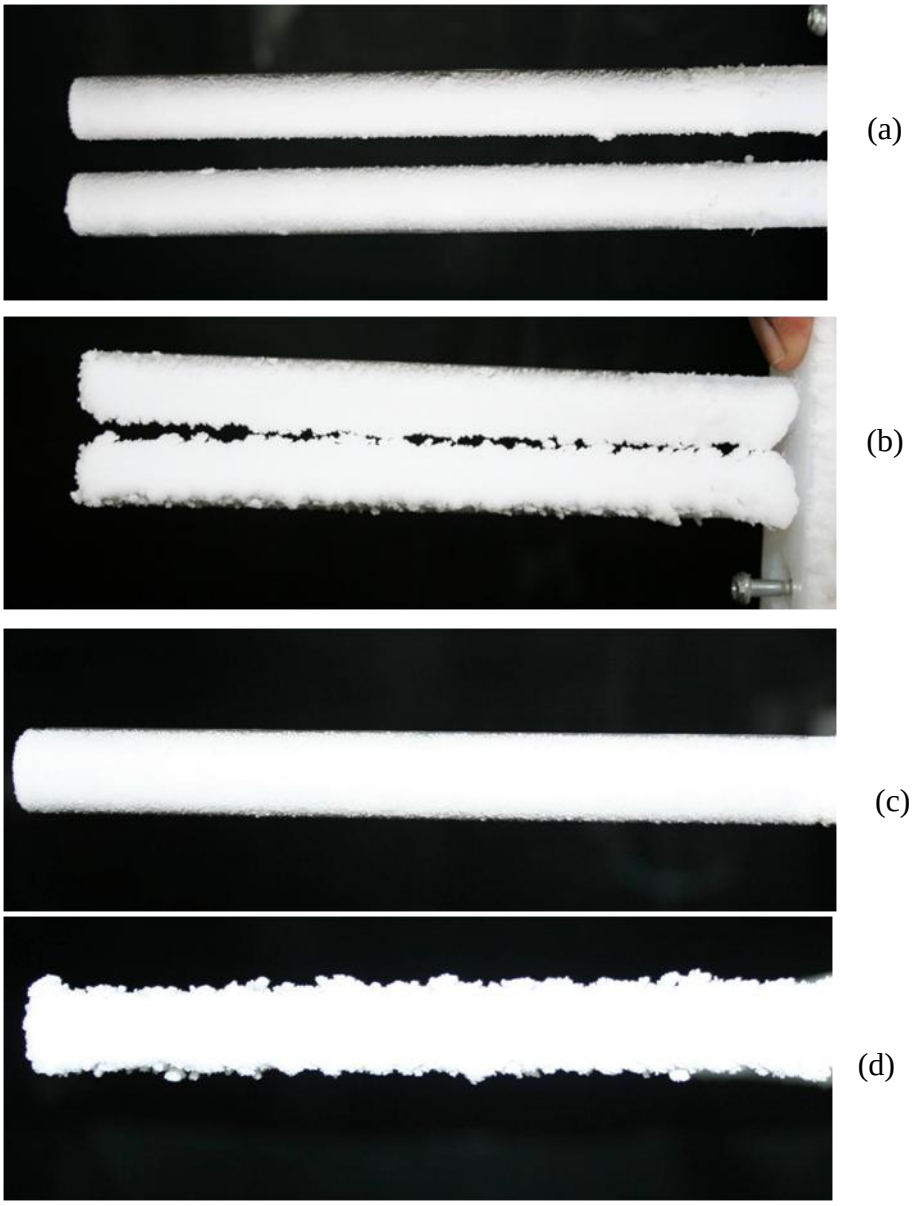

Figure 5.6: Photographs of rime ice formed on the cylindrical probes for parallel orientation (a and b) and inline orientation (c and d) at -10^{o}C, time 4 and 15 minutes respectively, wind speed of 5 m/s and LWC 0.8 g/m^{3}

(a) 3 minutes

(d) 10 minutes

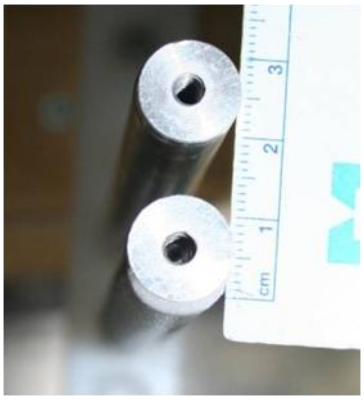

(b) 4 minutes

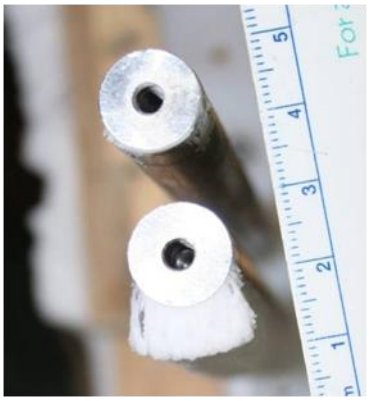

(e) 15 minutes

(c) 5 minutes

(f) 20 minutes

Figure 5.7: Top view time evolution of rime ice accretion on cylindrical probes for inline orientation at temperature of -10°C, wind speed 5 m/s and LWC 0.8 g/m^3

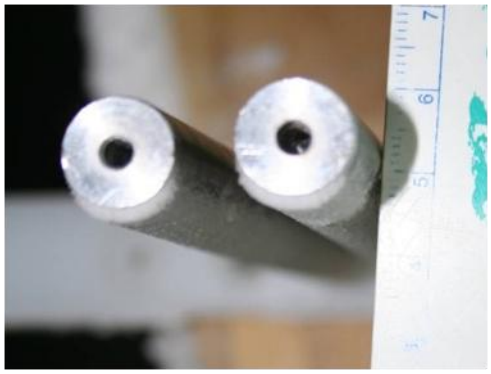

(a) 3 minutes

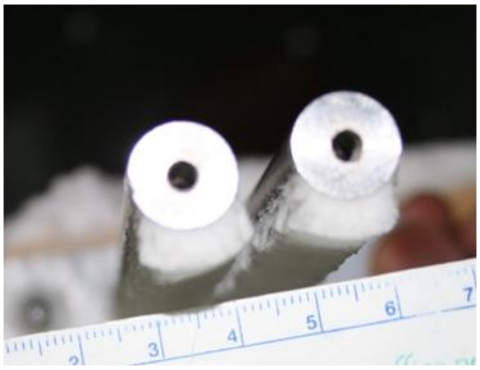

(d) 10 minutes

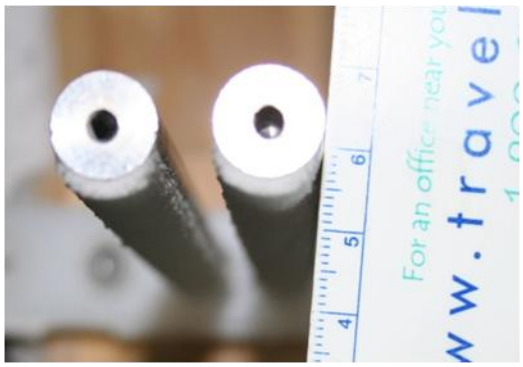

(b) 4 minutes

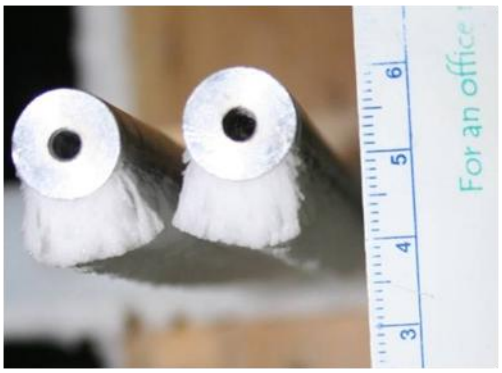

(e) 15 minutes

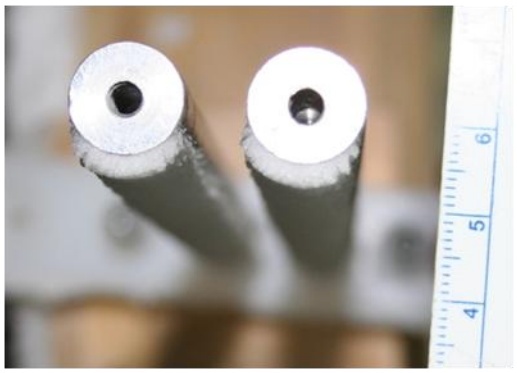

(c) 5 minutes

(f) 20 minutes

Figure 5.8: Top view time evolution of rime ice accretion on the cylindrical probes for parallel orientation at temperature of -10^{o}C, wind speed 5 m/s and LWC 0.8 g/m^{3}

5.3.2 Experiments at -2^{o}C

Glaze ice was formed on the probes, as shown in Figures 5.9 through 5.12, at -2^{o}C under relatively high liquid water content loading of 2 g/m^{3} in the icing wind tunnel. Since the rate at which heat is removed from the icing surface was not sufficient to freeze all impinging liquid water drops, i.e. an accretion efficiency < 1, a portion of the impinging drops dripped down the surface of the probe by gravity. The liquid water run-off gave rise to "horns" on the icing surface when they eventually froze. The distribution of the "horns" on the surface of the iced region appears to be a function of wind speed and the duration of the icing event for the inline orientation. As an example, the iced region for the inline orientation at 5 m/s was relatively smooth compared to 8 m/s and 10 m/s at the same time, as shown in Figure 5.9. At a higher air speed, the convective heat transfer is higher and the water drops cool more quickly on the probe surface. There were instances where the "horns" were observed predominantly on only one of the parallel oriented cylinders suggesting glaze ice growth was very sensitive to local wind velocity and orientation, as shown in Figure 5.10.

The cross-sectional shape of the accreted ice from the top view was generally convex with the radius of curvature increasing with time, as shown in Figures 5.11 to 5.12. For the parallel orientation, the accreted ice grew inwards towards each probe until they finally touched at the end of the longest test duration. The general appearance of the accreted ice was transparent under all test conditions.

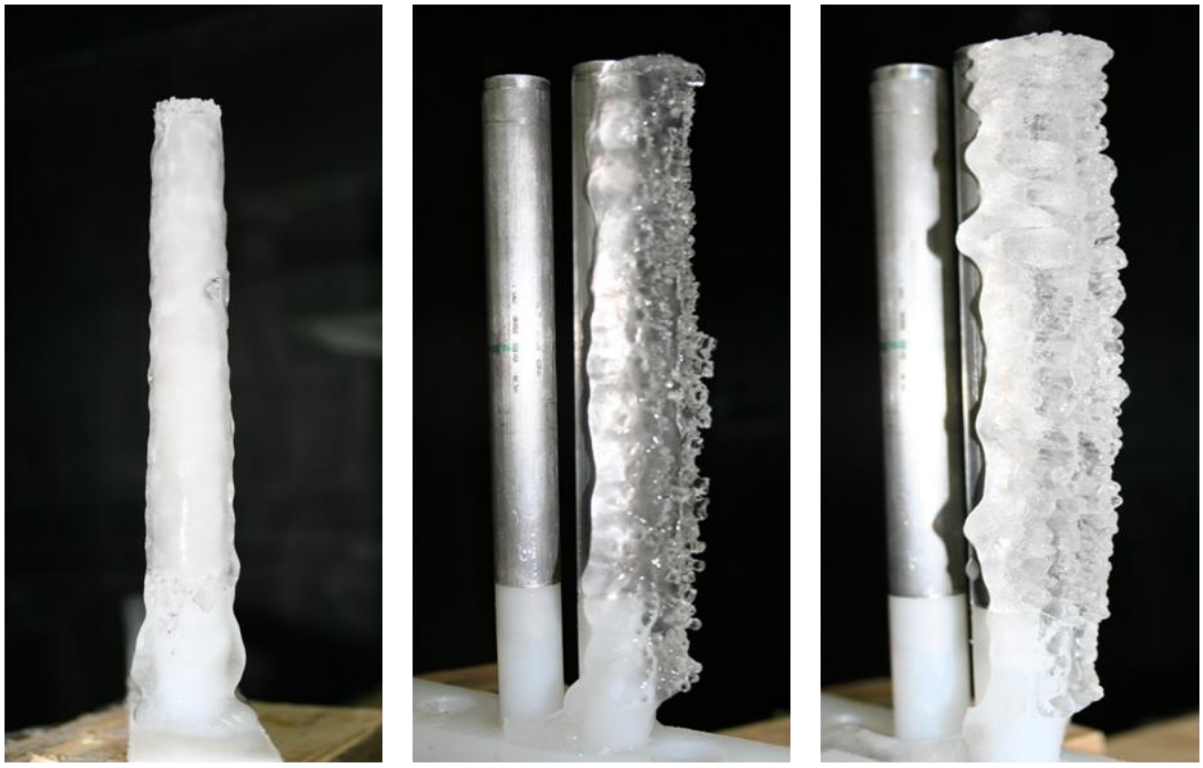

(a) 5 m/s (b) 8 m/s (c) 10 m/s

Figure 5.9: Compares horns on the iced region at various wind speeds after 20 minutes test, LWC 2 g/m^3

Figure 5.10: Glaze ice formation on cylindrical probes for the parallel orientation case with horn-like impressions predominant on the right probe

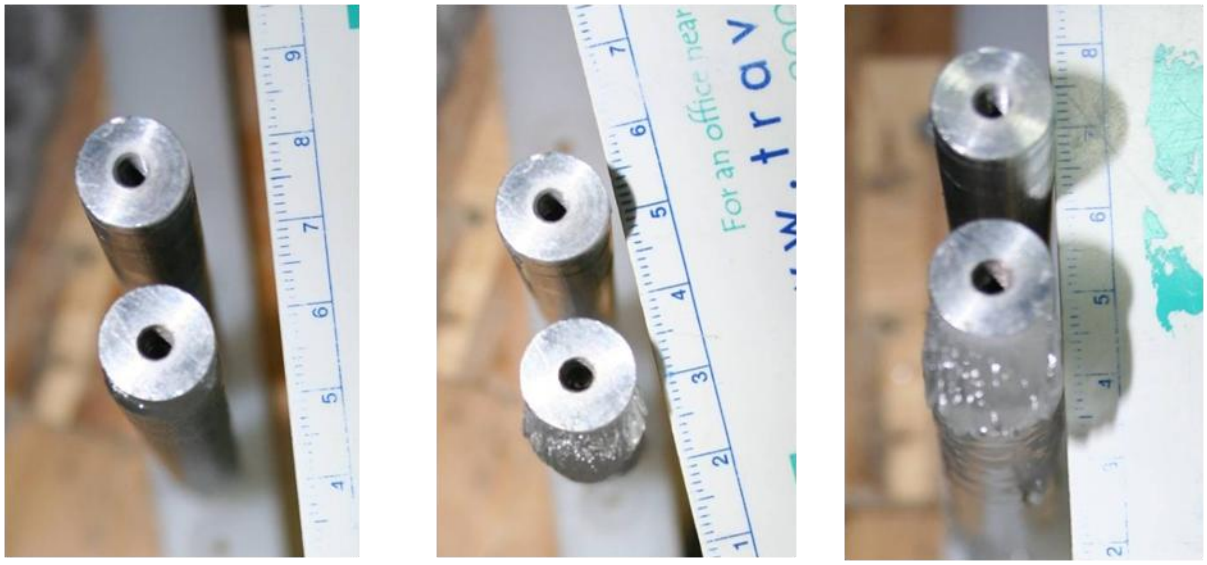

3 minutes 10 minutes 20 minutes

Figure 5.11: Top view time evolution of glaze ice accretion on the cylindrical probes for inline orientation at temperature of -2°C, wind speed 5 m/s and LWC 2 g/m^3

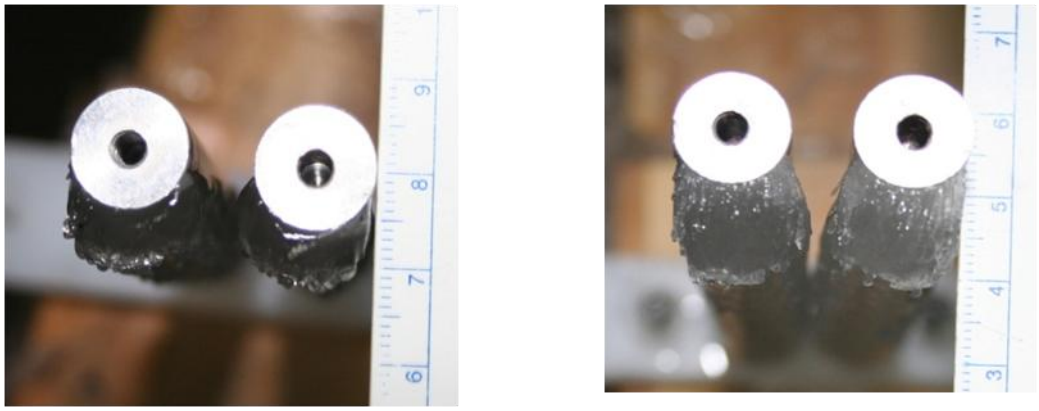

10 minutes 20 minutes

Figure 5.12: Top view time evolution of glaze ice accretion on the cylindrical probes for inline orientation at temperature of -2°C, wind speed 5 m/s and LWC 2 g/m^3

5.3.3 Ice accretion rate

The variation of mass and thickness of accreted ice on the cylindrical probes versus exposure time are shown in Figures 5.13 and 5.14, respectively. These tests were performed at three different wind speeds of 5, 8 and 10 m/s for both the inline and parallel orientation under rime and glaze icing conditions. The thickness and mass of ice accreted on the cylindrical probes increases approximately linear with the exposure time for all the wind speeds after the initial induction period from 0 to 3 minutes. The rate of icing of both rime and glaze ice are summarized in Table 5.2 for the various icing conditions. In each case, the icing rate was determined as the linear gradient of the curves in Figures 5.13 and 5.14. During either a rime or glaze icing event, the rate of icing determined increases as the wind speed increases. For example, under rime icing with the probe oriented inline, the rate of icing was 0.21 mm/s at 5 m/s velocity compared to 0.52 mm/s at 10 m/s. This result is in agreement with established equations for icing rate (Equation 2.1) where ice accretion is linearly proportional to velocity. Although the accretion efficiency of glaze icing is less than rime icing, higher accretion rates were observed for glaze icing. The higher rate was due to the larger impinging drop mass flux for the glaze icing cases.

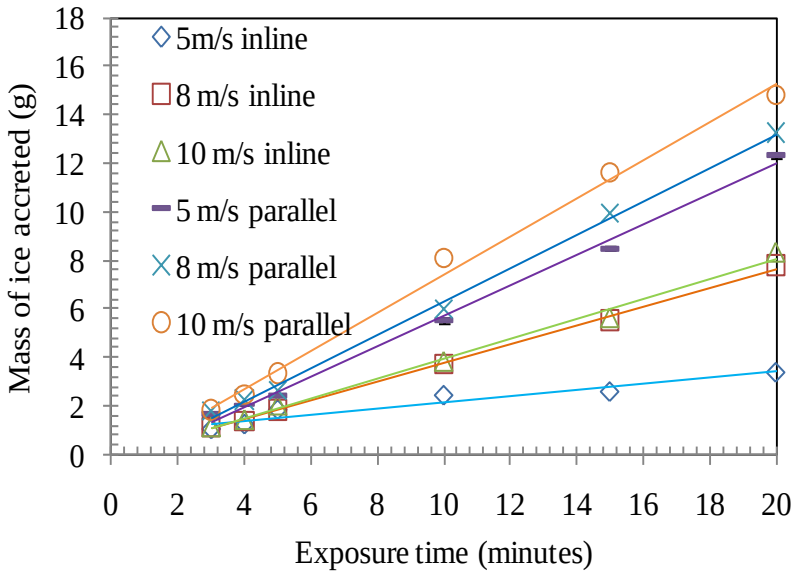

(a)

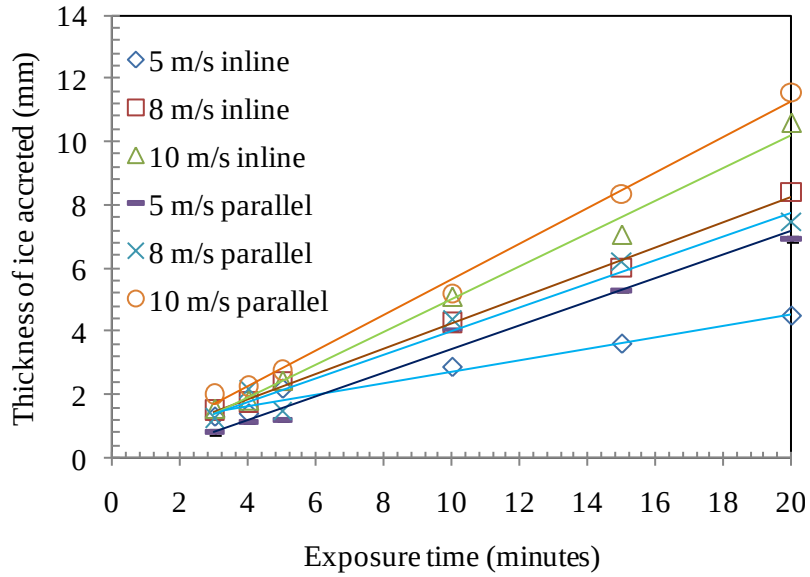

(b)

Figure 5.13: (a) Mass and (b) thickness variation with exposure time for rime ice at temperature of -10^{o}C and LWC 0.8 g/m^{3}, standard error bars on the 5 m/s parallel case

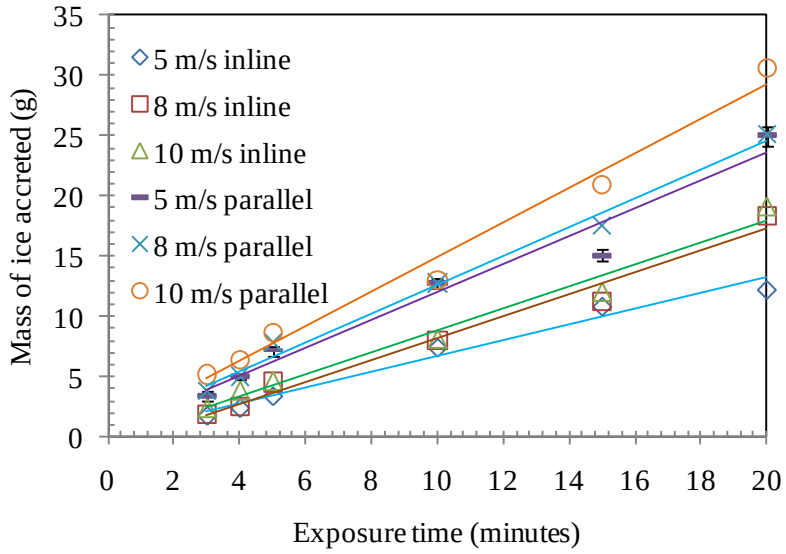

(a)

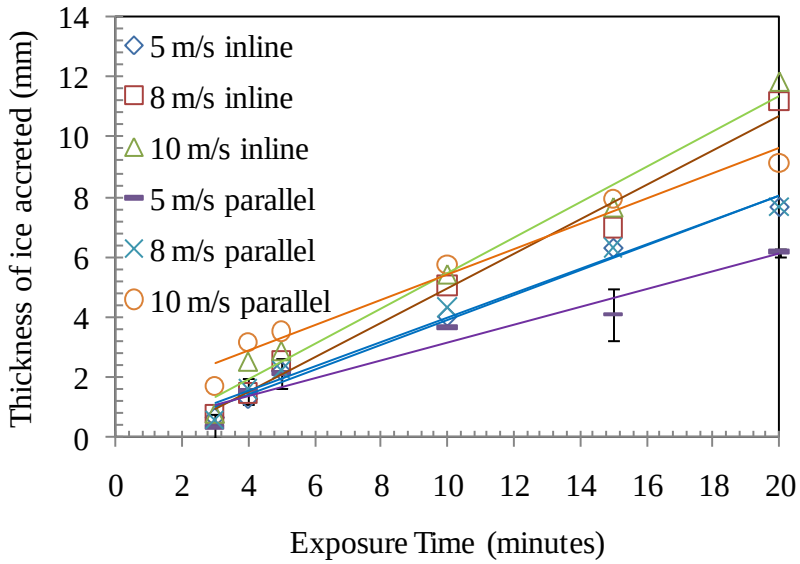

(b)

Figure 5.14: (a) Mass and (b) thickness variation with exposure time for glaze ice at temperature of -2^{o}C and LWC 2 g/m^{3}**,** standard error bars on the 5 m/s parallel case

Table 5.2: Summary of rate of icing on the cylindrical probes

Type of icing event	Orientation of probe	Wind speed (m/s)	Icing rate	
			Mass (g/s)	Thickness (mm/s)
Rime	Inline	5	0.15	0.21
		8	0.39	0.41
		10	0.41	0.52
	Parallel	5	0.61	0.36
		8	0.67	0.38
		10	0.77	0.57
Glaze	Inline	5	0.66	0.41
		8	0.89	0.55
		10	0.91	0.58
	Parallel	5	1.17	0.30
		8	1.21	0.40
		10	1.45	0.45

5.3.4 Capacitance variation with exposure time

Capacitance variation with exposure time was a critical parameter in determining the feasibility of the proposed measurement concept and optimal operating conditions. As the impinging

supercooled water drops enter the electric field, the capacitance changes. This change was due to the presence of impinging supercooled water drops and ice, whose dielectric constants differ from that of the ambient air. Since the dielectric constants of the impinging supercooled water drops and ice is greater than that of the ambient air, a general increment in the measured capacitance was expected. The capacitance variation with exposure time results are shown in Figures 5.15 and 5.16 for the rime and glaze ice cases, respectively.

As shown in Figure 5.15 for the rime ice case, the capacitance increased with exposure time and the measured capacitance was greater for the parallel orientation of the probes compared to the inline orientation. For the inline orientation, the percentage changes in capacitance over 20 minutes were 3.6%, 4.5% and 4.8% for velocities of 5, 8 and 10 m/s, respectively. Comparing these results with the corresponding changes in mass and thickness of the ice accreted, it is obvious that measured capacitance is weakly sensitive to ice accreted on the cylindrical probe. The explanation for this trend is as follows. The iced region for inline orientation sits in the weakest portion of the electric field, and ice deposits in this region will have relatively minimal effect on the measured capacitance. This trend is in agreement with simulations field results discussed in Section 5.1. The effect of wind speed on the measured capacitance was not obvious because the curves appear to lie on top of one another within the test duration. As observed above, the capacitance change with exposure time for the parallel orientation increased with exposure time but at a higher rate than the inline orientation. The capacitance results at different wind speeds were similar at shorter exposure times but diverge at longer exposure times. Comparing the mass and thickness of rime ice accumulated on the cylindrical probes, the similarity at shorter exposure time for the capacitance results might be due to the comparable accumulation of rime ice for the various wind speeds. The accumulation of rime ice at longer

exposure time however differs for the various wind speeds explored, and might be the cause of the divergence in the measured capacitance. For the parallel orientation, the percentage change in capacitance for 5, 8 and 10 m/s was 39.5%, 40.3% and 43.8%, respectively. These results compared to changes in mass and thickness indicates higher sensitivity of the measured capacitance to ice accretion than the inline orientation results. The results indicate, in agreement with the simulation filed results and acrylic experiments in Section 5.1, that the parallel orientation is more suitable for measuring capacitance change with ice accretion.

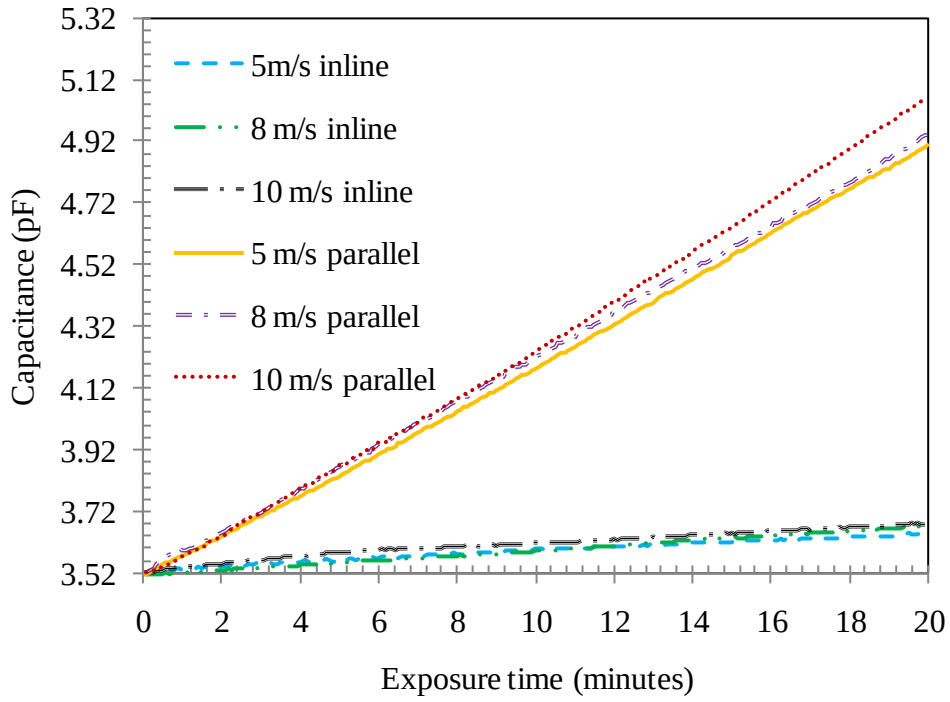

Figure 5.15: Capacitance variation with exposure time for rime ice at -10^{o}C, 0.8 g/m^{3}

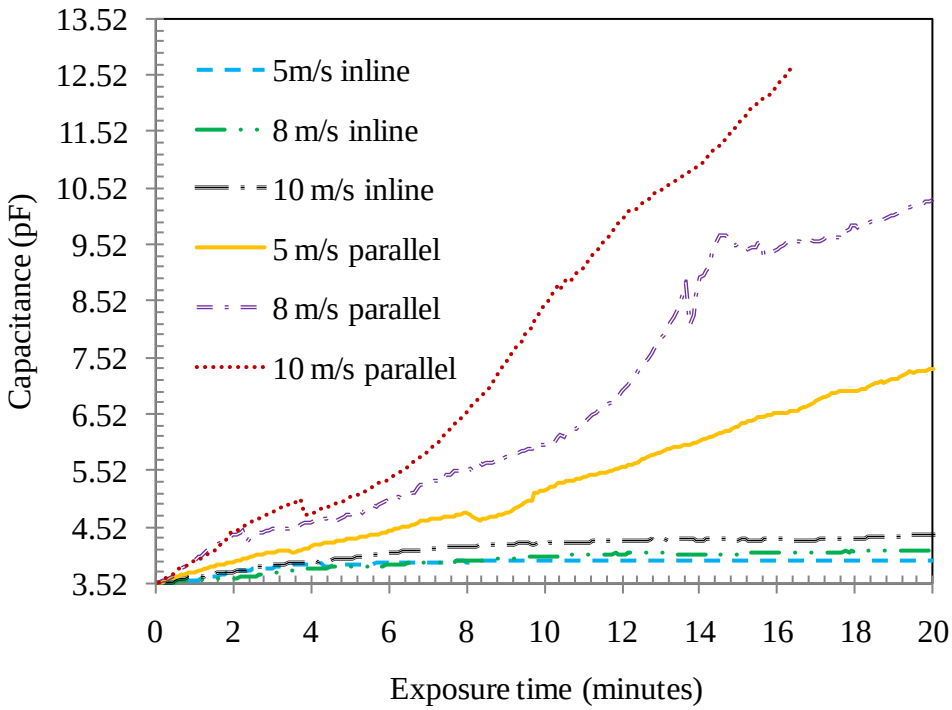

Figure 5.16: Capacitance variation with exposure time for glaze ice at -2^{o}C, 2 g/m^{3}

As shown in Figure 5.16 for the glaze ice case, the capacitance increased with exposure time and the measured capacitance was greater for the parallel orientation of the probes compared to the inline orientation. The change in capacitance for the inline orientation was small over all wind velocities considered. The percentage change in capacitance was 11.4%, 16.5% and 24.4% for velocities of 5, 8 and 10 m/s, respectively. As discuss above for the rime ice conditions, the low variation in capacitance is due to accretion of ice in a weak region of the probe's electric field. The effect of wind speed on the measured capacitance was not significant. This might be due to both the deposition of ice in the less sensitive region of the electric field, and the comparable accumulation (mass and thickness) of glaze ice. The change in capacitance was greater under glaze conditions compared to rime conditions because of the larger mass flux of water drops

under glaze ice conditions. The variation in capacitance with exposure time for the parallel orientation was very sensitive to wind velocity. In this case, it would be misleading to attribute this to differences in mass and thickness of glaze ice accumulated over the exposure time. More studies needs to be done to better explain this occurrence. During the 10 m/s test, the measured capacitance increased until the range of the meter was exceeded leading to overflow of the meter. This event was repeatable. From visual observation and photographs taken during this test, bridging of ice was noted at this point, and it is expect that the capacitance will be very large when bridging of ice occurs. This trend will not affect the ability of the probe since generally; the time to de-ice the wind turbine blades will be of the order of a few minutes.

5.3.5 Capacitance versus mass and thickness of ice accreted

The variation of capacitance with mass and thickness of ice accreted on the cylindrical probes for both rime and glaze ice conditions are showed in Figures 5.17 and 5.18, respectively. The results show a linear relationship between capacitance with both mass and thickness of ice accreted on the probe for both rime ice and glaze ice. This result is in agreement with Gerardi et al., [1993] particularly for capacitance variation with thickness. The capacitance increases more rapidly for the parallel orientation than the inline orientation because; the iced region for the parallel orientation is located in a more sensitive portion of the electric field. Additionally, the total amount of ice collected by the cylindrical probes when orientated parallel to the flow is greater than when oriented inline to the flow which also increases sensitivity of the sensor.

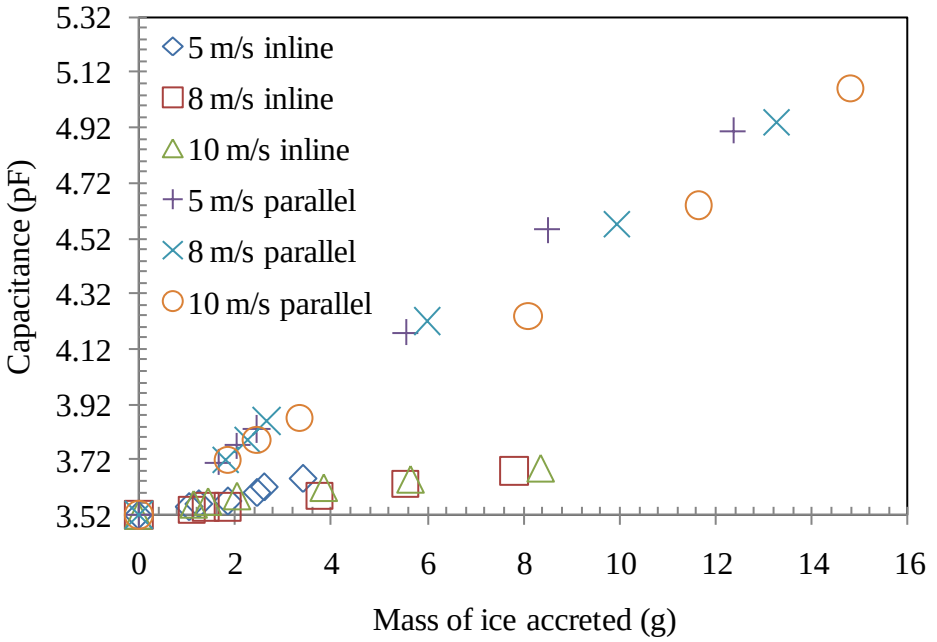

(a)

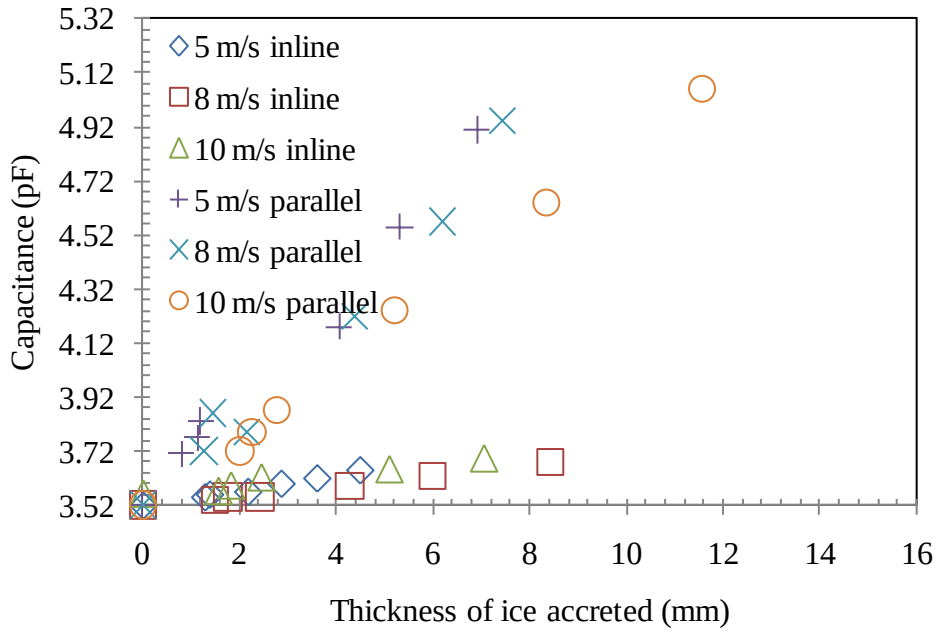

(b)

Figure 5.17: Capacitance variation with (a) mass and (b) thickness respectively for rime ice conditions at various wind velocities at temperature -10^{o}C and LWC 0.8 g/m^{3}

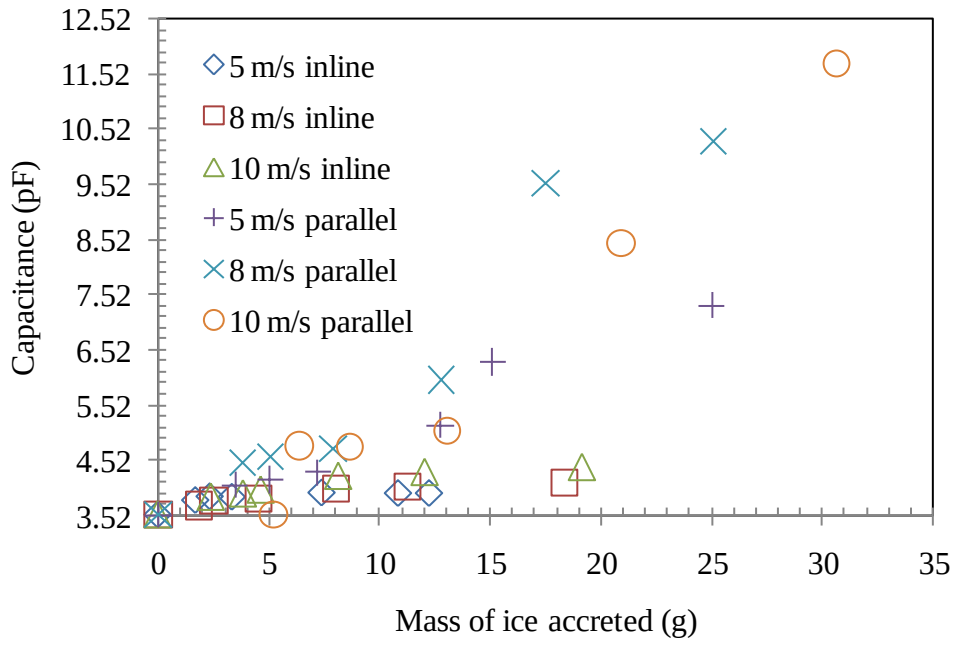

(a)

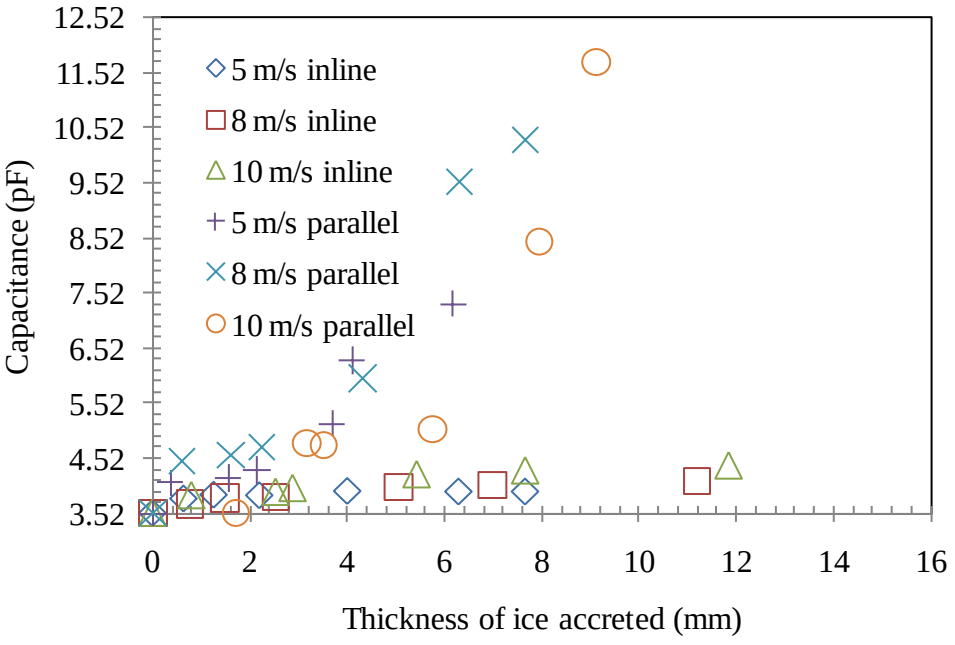

(b)

Figure 5.18: Capacitance variation with (a) mass and (b) thickness respectively for glaze ice at various wind velocities at temperature -2^{o}C and LWC 2 g/m^{3}

5.3.6 Sensitivity

Capacitance normalized with mass and thickness versus exposure time is shown in Figure 5.19 and Figure 5.20 for both rime and glaze ice, respectively. Rime ice curves indicate a sharp increase in the normalized capacitance with exposure time during the first few minutes (3 to 5 minutes) after which the curves plateaus especially for the inline orientation. For the parallel orientation case, there were a few variations in both capacitance per mass and capacitance per thickness, as seen in Figure 5.19. This initial trend implies the sensor is more sensitive within the first few minutes of icing events for rime ice. This high sensitivity in the initial stages of an icing event would allow early implementation of wind turbine blade de-icing strategies under sever icing conditions. However, the flat trend after the initial stage is equally of importance especially in predicting ice type. This is because observations of time dependent ice growth photographs from the wind icing experiments indicate slight variation in ice structure within these periods. These trends are similar to when the glaze ice event was simulated in the icing wind tunnel as shown in Figure 5.20. For both rime and glaze ice events, there was poor correlation between thickness and capacitance.

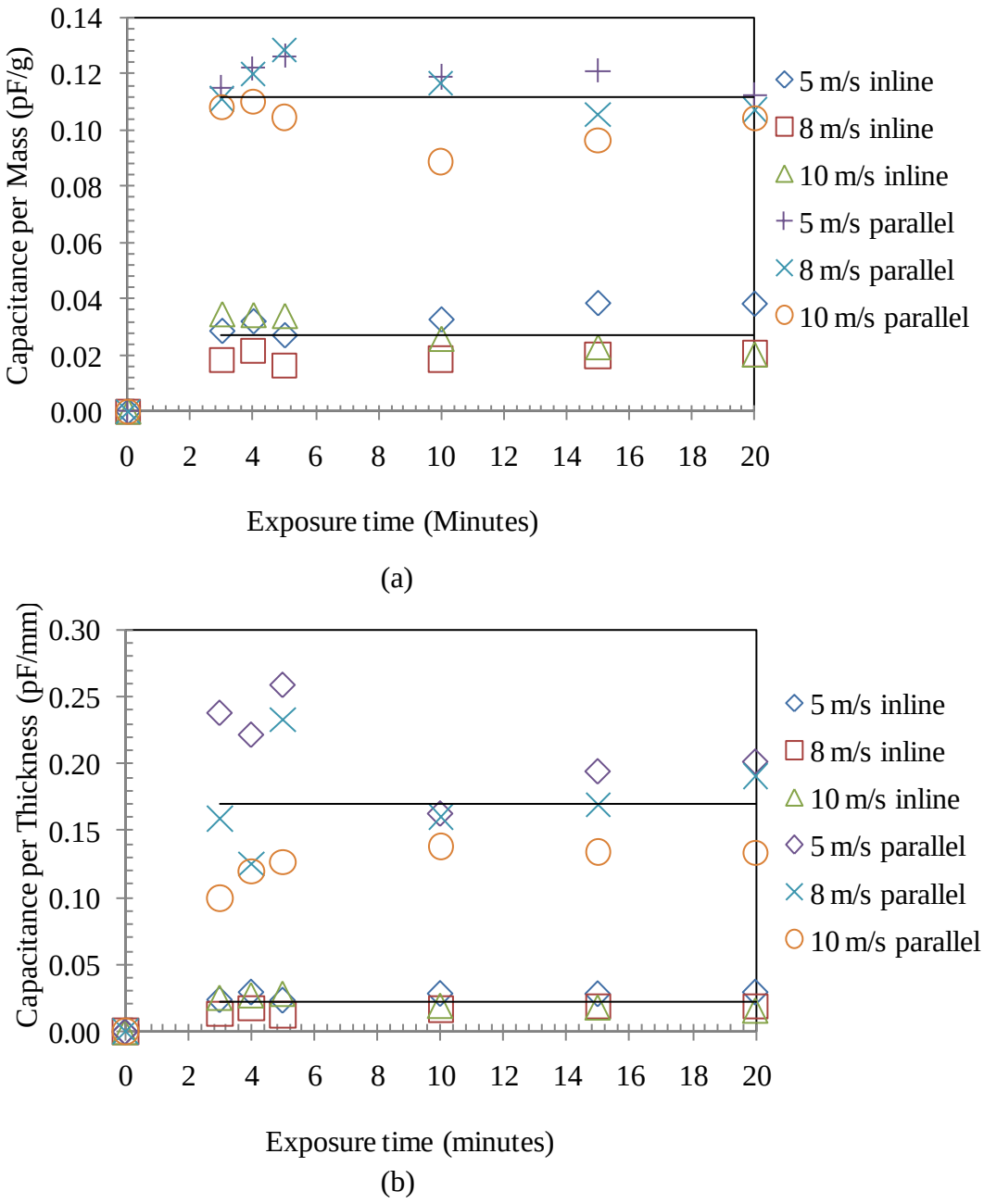

Figure 5.19: Capacitance normalized with (a) mass and (b) thickness respectively versus exposure time for rime ice at various wind velocities at temperature -10^{o}C and LWC 0.8 g/m^{3}

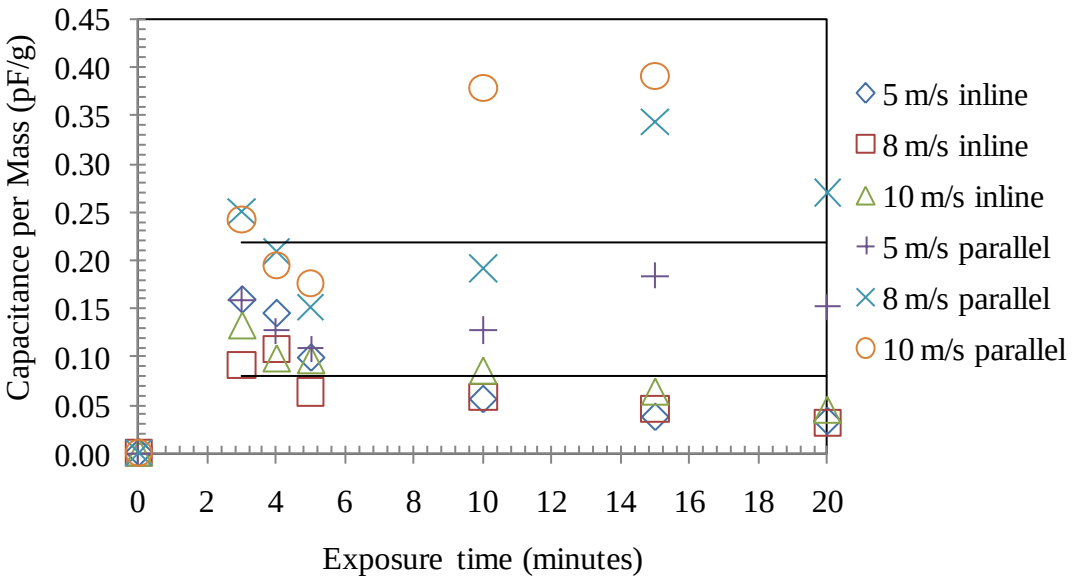

(a)

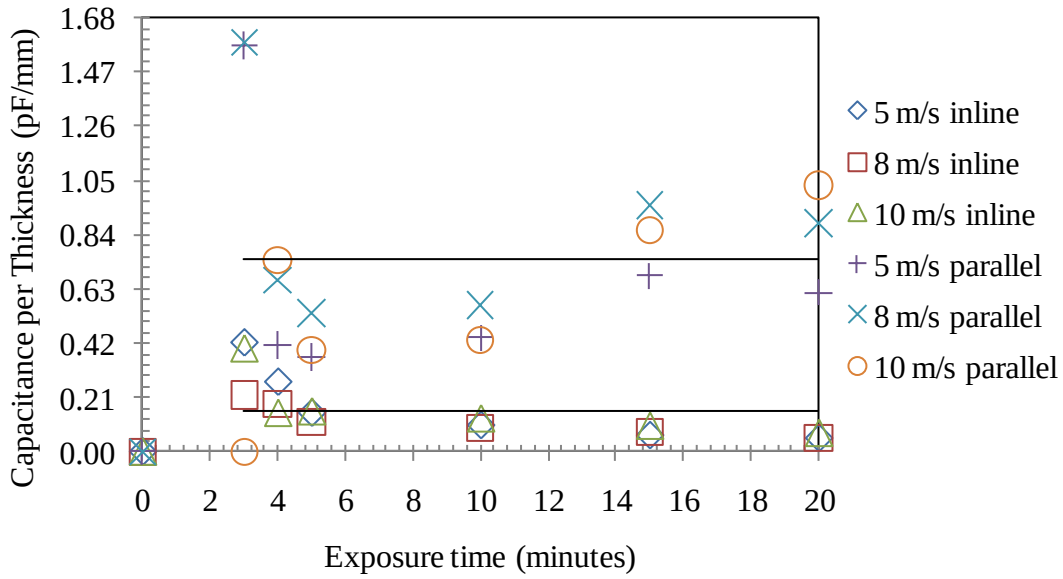

(b)

Figure 5.20: Capacitance normalized with (a) mass and (b) thickness respectively versus exposure time for glaze ice, at various wind velocities at temperature -2^{o}C and LWC 2 g/m^{3}

5.3.7 Resistance change against exposure time

Changes in the measured capacitance with exposure time during the icing experiments as previously discussed was due to differences in dielectric constants that could be attributed to variation in the matrix of ice, air and supercooled water drops deposited on the iced region of the probe. For this reason, the output capacitance recorded for both icing events gave an indication of ice accretion type on the surface of the cylindrical probes. Therefore based on the capacitance results, it would not be possible to decipher between the two icing events simulated in the icing wind tunnel. Hence, to distinguish between rime and glaze ice in the icing wind tunnel, another technique based on resistance measurements is proposed. The inline orientation was not considered for the changes in resistance since the deposit is not between the cylindrical probes.

As ice deposits on the front face of the cylindrical probes, there is interaction with the electric field as discussed earlier. Additionally, the air gap between the cylindrical probes decreases as the accreted ice grows. Consequently, the resistance decreases with time for both the rime and glaze ice conditions. Figure 5.21 shows an exponential decay rate for both icing events. It was noted that the decay rate was slower for rime ice compared to glaze ice. This phenomenon was explained as follows. Electric fields interact with the surface of the substance without penetrating thereby eliminating any contributions from the internal structure of the accreted ice. Thus, the conditions prevailing on the surface of the probe undergoing rime and glaze icing is paramount to this trend. Glaze ice as discussed earlier, is characterised by water run-offs on the surface, while the surface of rime ice is “dry” i.e. no water run-offs. Air has a higher resistance to electric flow than water leading to the relatively slow decay of the measured resistance for rime ice compared to glaze ice. Therefore, the decay rate was used to assert the type of in-cloud icing event in our proposed method. It should be noted that the higher liquid content involved in glaze

ice formation might have aided the decay rate. However, it can be argue that, under the same liquid water conditions, there will be water run-offs on the surface of glaze ice because of its unique formation process, while rime ice on the other hand will have a dry surface also due to its characteristic formation process and, a relatively higher decay rate for glaze ice compared to rime ice will be observed.

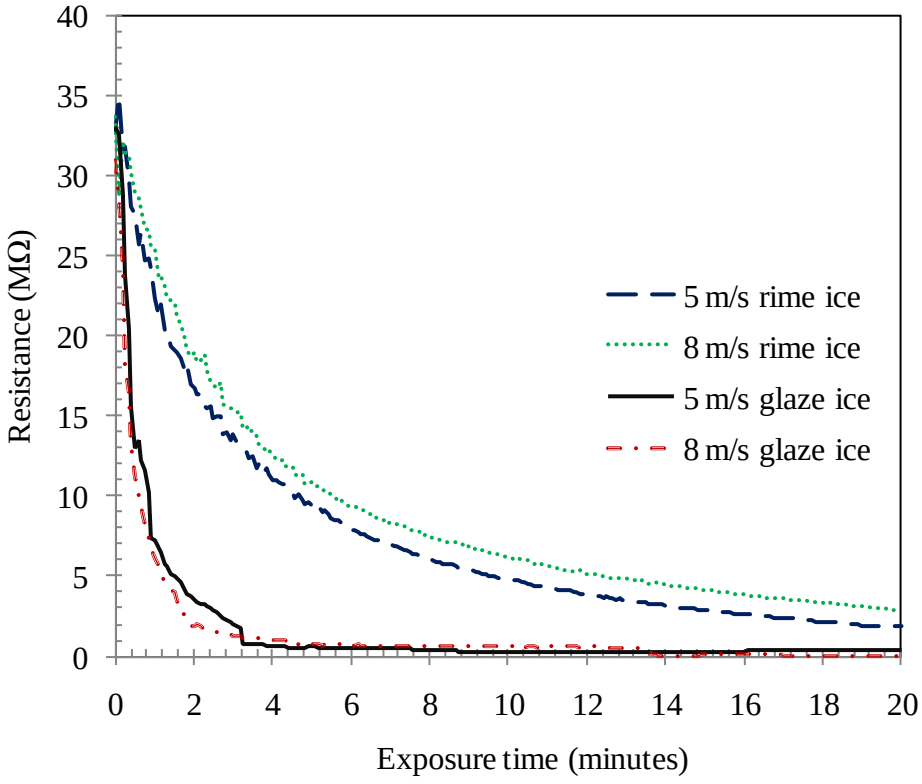

Figure 5.21: Resistance variation with exposure time

5.4 Proposed sensor configuration

The results presented in this chapter demonstrate the feasibility of this sensor for ice detection. Based on the conditions considered in this study, a summary of the optimal dimensions and the best orientation of the cylindrical probes to supercooled water drops are listed in Table 5.3.

Table 5.3: Optimal sensor configuration

Length of cylinder (cm)	15
Number of cylinders	2
Center-to-center, s (cm)	1.87
Diameter, d (cm)	1.27
Orientation to supercooled water drops	Parallel

This study suggests that an ice accretion measurement device developed based on the capacitance/resistance concept would be suitable for placement on meteorological towers or the nacelle of wind turbines. Ice accretion on wind turbine blades is expected to be different than that measured near the blades, however the ice accretion rate data is expected to provide useful information for anti-icing and de-icing strategies.

.

Chapter 6

Conclusions

6.1 Conclusions

Wind power production in ice prone regions is hindered by icing of wind turbines. Problems associated with icing of wind turbines vary, and they all require removal of ice from the surface of the wind turbine blades. In this research, an ice sensor base on a novel concept suitable for measuring ice accretion on meteorological metrological towers near wind farms and nacelles of wind turbines are demonstrated numerically and experimentally in a laboratory setting. This concept is based on the changes in measured capacitance and resistance with ice accretion. Two orientations of the ice sensor to supercooled drops laden wind, inline and parallel, under simulated rime and glaze icing events in the wind icing tunnel, are analyzed.

Results from the numerical studies indicate that, the sensitivity of the ice sensor was a function of the center-to-center distance between the cylindrical probes, the sizes of the cylindrical probes, and the location of the ice deposition. The sensitivity of the ice sensor decreases with increasing center-to-center distance. Additionally, two different sized cylindrical probes were found to be less sensitive to icing compared to cylindrical probes of the same size. Finally, with both the center-to-center distance and the diameter of the cylindrical probes fixed, modelled ice deposition on the front surfaces of both cylindrical probes (parallel orientation) was more sensitive than the case where the modelled deposition was on the side of only one of the cylindrical probes (inline orientation). The high sensitivity for the parallel orientation case was observed in the wind icing tunnel experiments. The high sensitivity for the parallel orientation case implies preferentially orienting the cylindrical probes to the flow direction.

From the wind icing tunnel experiments, the icing rate was found to be relatively constant indicating little or no change in the aerodynamics of the flow for both icing events after the initial induction period. The calculated icing rates were found to increase with wind speed. The measured capacitance, which gave an indication of an icing event, was observed to increases with exposure time and ice deposition. The sensitivity of the ice sensor to ice deposition was found to be high within the first few minutes (typically between 3 and 5 minutes) of exposure, after which the curves level off. This high sensitivity of the sensor within the few minutes of exposure is advantageous, since it would allow quick remedial action to the ice deposition on the wind turbine blade. The flat trend after the initial stage is equally of importance especially in predicting icing structure, since observations during the experiments indicate slight variation in ice structure. It was not possible to categorically discriminate between rime and glaze icing events exclusively based on the results from the measured capacitance and to do this, resistance results were used. The resistance decreases exponentially with ice accretion, with resistance for the glaze ice case decaying faster than for the rime ice case. For both icing events, the decay was towards an asymptotic value.

Chapter 7

Recommendations

7.1 Recommendations

This study suggests that an ice accretion measurement device developed based on the capacitance/resistance concept would be suitable for placement on meteorological towers or the nacelle of wind turbines. The device could detect an icing event, mass accretion of ice and differentiate between rime and glace icing events. However, there are more steps required in order to commercialise this sensor. In this light, the following are recommended for future investigations.

- Testing the sensor under a wider variation of liquid water contents (LWC).
- Testing the sensor under a wider variation of wind speeds.
- Testing the sensor under a wider variation of temperatures.
- Testing the sensor in real icing conditions and results compared with existing sensor.
- Testing the sensor under the other types of icing events not explored in this work e.g. freezing rain, mixed rime and glaze etc.
- Develop a de-icing system for the sensor.
- Investigate if melting time during de-icing of sensor can correlate to ice thickness.
- Investigate the significant effect of changing the field frequency to detect the onset of water deposition on the probe.

Reference

Admirat, P., Sakamoto, Y.,1988, "Wet Snow on Overhead Lines: State-of-Art," *Proc. 4th Int. Workshop on Atmospheric Icing of Structures*, pp. 8-13.

Ahmed W.H., Ismail, B.I., 2008, "Innovative Techniques for Two-Phase Flow Measurements," *Recent Patents on Electrical Engineering*, vol.1 no.1, pp. 1-13.

Ahti, K., Makkonen, L., 1982, "Observations on Rime Formation in Relation to Routinely Measured Meteorological Parameters," *Geophysica* vol. 19, pp. 75–85.

Bose, N., 1992, "Icing on a Small Horizontal Axis Wind Turbine-Part 1: Glaze Ice Profiles," *Journal of wind engineering and industrial aerodynamics*, vol. 45, pp. 75-85.

CanWEA, "Wind Generation to Experience Strong Growth," Windlink, January 9, 2007, Issue no. 6.

CanWEA, "Wind Vision 2025 Powering Canada's Future," 2008. <http://www.windtrm.gc.ca/pdfs/windvision_summary_e.pdf>. accessed 19th December 2009.

Chamuel, J.R., 1984, "Ultrasonic Aircraft Ice Detector using Flexural Waves" United States Patent number 4,461,178.

Paul, C., 2000, Fundamentals of Electric Circuit Analysis, *John Wiley & Sons. Inc.*, 605 Third Avenue, New York, NY 10158-0012.

COST 727, 2006, "Atmospheric Icing on Structures-Measurement and Data Collection on Icing: State of The Art," *A compilation of the contributions of the Working Group 2 participants*.

Craig, D.F., Craig, D.B., 1995, "An Investigation of Icing Events on Haeckel Hill," Proceedings *of BOREAS III Conference*, Finland.

Crowe, T.C., Sommerfeld, M., Tsuji, Y., 1998, Multiphase Flows with Droplets and Particles *CRC Press*, Boca Raton, Florida.

DeAnna, R., 1999, "Ice Detection Sensor," United States Patent number 5,886,256.

Drage, A., Lange, T.D., 2005, "Instruments for Measuring Atmospheric Icing,'' Reports in Meteorology and Oceanography.

Ducu, D.O., Donahue, R.J., Ghandhi, J.B., 2001, "Design of Capacitance Probes for Oil Film Thickness Measurements Between the Piston Ring and Liner in Internal Combustion Engines," *Journal of Engineering for Gas Turbines and Power*, vol. 123, no. 3, pp. 633-643.

Elkow, K.J., Rezkallah, K.S., 1996, "Void Fraction Measurements in Gas-Liquid Flows using Capacitance Sensors," *Measurement Science and Technology*, vol. 7, pp. 1153-1163.

Federow, H.L., Silverman, J.H., 1994, "Laser Ice Detector," United States Patent number 5,296,853.

Frohboese, P., Anders, A., 2007, "Effects of Icing on Wind Turbine Fatigue Loads," *IOP Publishing Journal of Physics: Conference Series*, Copenhagen.

Ganander, H., Ronsten, G., 2003, "Design Load Aspects due to Ice Loading on Wind Turbine Blades," *Proceedings of the BOREAS VI Conference*, Finland.

Geraldi, J.J., Hickman, G.A., Khatkhate, A.A., Pruzan, D.A., 1996, "Measuring Ice Distribution Profiles with Attached Capacitance Electrodes," United States Patent number 5,551,288.

Goldberg, J.L., Lardiere Jr., B.G., 1993, "Expulsive Ice Detector," United States Patent number 5,523,959.

Goodrich 0871LH1 Freezing Rain Sensor Instrumentation Manual, Goodrich, 2008.

Hansman Jr., R.J., Kirby,M., "Measurement of Ice Growth during Simulated and Natural Icing Conditions using Ultrasonic Pulse-Echo Techniques," *Journal of Aircrafts* vol. 23 pp. 492-498.

HIOKI 3522-50 LCR HiTESTER Instruction Manual, HIOKI.E.E. Corporation, Japan, 2007.

Homola, C.M., Nicklasson, P.J., Sundsbø, P.J., 2006, "Ice Sensors for Wind Turbines," *Cold Regions Science and Technology* vol. 46, pp. 125-131.

Infralytic "Ice Sensor for Rotor Blades," < www.infralytic.de>. accessed 25th May 2010.

Jasinski, W.J., Noe, S.C., Selig, M.S., Bragg, M.B., 1998, "Wind Turbine Performance under Icing Conditions," *Transactions of the ASME, Journal of Solar Energy Engineering*, vol. 120, pp. 60-65.

Kaiser, K.L., 2000, Electromagnetic Compatibility Handbook, *CRC Press*, Boca Raton, Florida.

Khurgin, B., "Ice Detector with Movable Feeler," United States Patent number 4,873,510, 1989.

Kimura, S., Tammelin, B., Santti, K., 2000, "Estimation of reduction of power production due to icing from existing meteorological data," *BOREAS V*, Finland.

Klainer, S.M., Milanovich, F.P., 1990, "Optical Sensor for the Detection of Ice Formation and other Chemical Species," United States Patent number 4, 913,519.

Kraj, A. G., 2007, "Icing Characteristics and Mitigation Strategies for Wind Turbines in Cold Climates," *M.Sc thesis*, University of Manitoba.

Laakso, T., Holttinen, H., Ronsten, G., Tallhaug L., Horbaty, R., Baring-Gould, I., Lacroix, A., Peltola, E., Tammelin, B., 2003, "State-of-the-Art of Wind Energy in Cold Climates." *International Energy Agency, Annex* XIX, Finland.

Labkotec Ice Detectors LID 33210C User Manual, Labkotec Oy, Finland, 2009.

Labkotec Ice Detectors LID 33210D User Manual, Labkotec Oy, Finland, 2003.

Lardiere Jr., B.G., Wells, B.F., 1998, "Integrated Planar Ice Detector" United States Patent number 5,790,026.

Lee, H., Seegmiller, B., 1996, "Ice Detector and De-icing Fluid Effectiveness Monitoring System," United States Patent number 5,523,959.

Louge, M.Y., Steiner, R., Keast, S.C., Decker, R., Dent, J., Schneebeli, M., 1997, "Application of Capacitance Instrumentation to the Measurement of Density and Velocity of Flowing Snow," *Cold Regions Science and Technology*, vol. 23, pp. 47-63.

Louge, M.Y., Foster, R.L., Jensen, N., Patterson, R., 1998, "A Portable Capacitance Snow sounding Instrument", *Cold Regions Science and Technology*, vol. 28, pp. 73-81.

Maatuk, J., 2004 "Microprocessor-based Liquid Sensor and Ice Detector," United States Patent number 6,776,037.

Magenheim, B., 1977, "Microwave Ice Detector," United States Patent number 4,054,255.

Makkonen, L., 2000, "Models for the Growth of Rime, Glaze, Icicles and Wet Snow on Structures," *Philosophical Transactions: Mathematical, Physical and Engineering Sciences*, vol. 358, no. 1776, pp. 2913-2939.

Makkonen, L., 1984, "Modelling of Ice Accretion on Wires," *Journal of Climate and Applied Meteorology*, vol. 23, issue 6, pp. 929-939.

Patel, M.R., 2006, Wind and Solar Power System; Design, Analysis and Operation, Second Edition, *CRC Press*, Florida.

Piazza, R., Parola, A., 2008, "Thermophoresis in Colloidal Suspensions," *Journal of Physics: Condensed Matter*, vol. 20.

OuickField™ User Guide Version 5.3, Tera Analysis Limited, Denmark, 2005.

Reid, W.T., 1971, External Corrosion and Deposits-boilers and Gas Turbines, *American Elsevier Publishing Company*, New York.

Seifert,H., 2003, "Technical Requirements for Rotor Blades Operating in Cold Climates," *proceedings of the BOREAS II conference* Pyhätunturi, Finland.

Vibro-meter " Vibro-meter.com/aerospace/ice.html" accessed 25th May 2010.

Wakahama, G., Kuroiwa, D., Goto, D., 1977, "Snow Accretion on Electric Wires and its Prevention," *Journal of Glaciology* vol. 19, no. 81, pp. 479–487.

Wallace, R.D., Gillespie, A.B., Sweet, D.B., Rauckhorst, R.L., Terry, M.J., Holyfield, M.E., 2002, "Ice Thickness Detector," United States Patent number 6,384,611.

Wang, X., 2008, "Convective Heat Transfer and Experimental Icing Aerodynamics of Wind Turbine Blades," *Ph.D thesis*, University of Manitoba.

Wimmer, R., Kranz, M., Boring, S., Schmidt Albrecht, 2007, "A Capacitive Sensing Toolkit for Pervasive Activity Detection and Recognition," *Proceedings of the fifth IEEE International Conference on Pervasive Computing and Communications*, pp. 171-180.

Rondeau, J., "Rondeau Opens National Wind Energy Conference," Winnipeg Canada. 23rd October, 2006. < http://news.gov.mb.ca/news/index,print.html?archive=&item=178>. accessed 20th November 2009.

Robinson, D.A., Gardner, C.M.K., Evans, J., Cooper, J.D., Hodnett, M.G., Bell, J.P., 1998, "The Dielectric Calibration of Capacitance Probes for Soil Hydrology using an Oscillation Frequency Response Model," *Hydrology and Earth System Sciences*, vol. 2, pp. 83-92.

Rocha, M.S., Cabral, E.L.L., Simões-Moreira, J.R., 2009, "Capacitance Sensor for Void Fraction Measurement in a Natural Circulation Refrigeration Circuit," *International Nuclear Atlantic Conference*, Brazil.

RMS., 2008, "The 1998 Ice Storm: 10-year Retrospective," Report by Risk Management Solutions (RMS), Inc.

Ryerson, C.C., 2008, "Assessment of Superstructure Ice Protection as Applied to Offshore Oil Operations Safety: Problems, Hazards, Needs, and Potential Transfer Technology," US Army Corps of Engineers, *Cold Regions Research and Engineering Laboratory*.

Appendix A

Liquid Water Content Estimation

Two approaches were used to determined the liquid water content (LWC) in the Icing Wind Tunnel for both rime and glaze ice.

In the first approach, it was assumed that the spread of the liquid cloud fills the entire cross-sectional area of the working section (i.e. inner duct) of the Icing Wind Tunnel with no boundary layer formation on the inner walls of the duct. With this assumption in place, the mass flow rate through the entire cross-sectional area of the inner duct was calculated from the flow rate peculiar to the type of ice whose LWC is been determined and density of water. Next, the volumetric flow rate through the entire inner duct was computed from the velocity and the cross-sectional area of the inner duct. With these two values, the LWC was then calculated and listed in Table A.1.

The second approach determined the LWC based on estimating the cross-sectional area of the liquid cloud through measurement of the extent of ice deposition on a horizontally and vertically oriented rod. This method assumes that all water drops in the path of the rod hit and stick to the rod and that the water drop distribution is uniform over the measured area. The experimental procedure followed was:

1. Mount a long cylindrical rod in a horizontal orientation icing spanning the entire width of the working section (i.e. the inner duct).
2. Run the icing wind tunnel until a stable temperature of -10 °C and air velocity of 5m/s is achieved.
3. Turn on the sprayers and quickly adjusted to the required conditions for rime ice.

4. Turn sprayers off after 15 minutes.
5. Measure the length of the iced section of the rod.
6. Orient the rod vertically and repeat steps 2 to 5.
7. Calculate the cross-sectional area of the liquid cloud. Calculate LWC form the mass flow rate and the cross-sectional area of the liquid cloud.

The area was estimated in two ways and with these areas known, the LWC was estimated as described above. Table A.1 shows the results for the LWC based on these two areas.

Table A.1: Estimated LWC values

Type of Ice	**LWC (g/m^3)**	
	First Approach	Second Approach
Rime Ice	0.4	0.8
Glaze Ice	1.3	2.0

The first approach based on the dimensions of the Icing Wind Tunnel underestimates the LWC compared to the measured results, i.e. the second approach. During the experiments, it was

observed that the amount of ice deposited on the rod varied across the length of the rod, which would tend to underestimate the LWC as would the assumption of 100% capture efficiency. The values from the second approach were quoted in this research.

Appendix B

Ice detector methods

Table B.1: Indirect methods of ice detection (Homola et al., 2007)

Study	Concepts
Craig and Craig, 1995	Variations in the speeds of a heated and unheated anemometers
Seifert, 2003	Variations in the cycles per second of noise emanating from wind turbine
Makkonen et al., 2005	Measurement of temperature and dew point of winter weather
Laakso et al., 2003	Variations in the power calculated using the wind speed against actual power from the wind turbine
Laakso et al., 2003	Variations in the resonant cycles per second of wind turbine blades

Table B.2: Direct methods of ice detection

Study/Company	**Concept**
Labkotec Oy, 2009	Ultrasonic principle
Chamuel, 1984	Ultrasonic principle
Wallace et al., 2002	Measurement of electrical impedance
Lee and Seegmiller, 1996	Measurement of electrical inductance
Geraldi et al., 1996	Measurement of capacitance
Maatuk, 2004	Effect of phase change on an icing surface
Lardiere and Wells, 1998	Monitoring the behaviour of a material with temperature
Goodrich, 2008	Magnetostrictive principle
Vibro-Meter, 2005	Measurement of piezoelectric effects
Magenheim, 1977	Transmission and monitoring of a low microwave signal into a layer of dielectric material
Federow and Silverman, 1994	Detection of refracted light along the surface of a plastic by a photo detector
Klainer and Milanovich, 1990	Variation in the optical properties of ice and water
DeAnna,1999	Movement or non-movement of a diaphragm due to water or ice covering it
Gerardi et al., 1993	Capacitance change

Study/Company	Concept
Ryerson, 2008	Analysis of infrared red signal
Infrarlytic, 2005	Differences in absorbing properties of materials
Khurgin, 1989	Covering an aperture by ice
Laakso et al., 2003	Infrared beam
Seifert, 2003	Monitoring via camera
Hansman and Kirby, 1986	Ultrasonic principle
Laakso et al., 2003	Impedance and temperature measurement
Laakso et al., 2003	Monitoring of ice build on load cells
Goldberg and Lardiere, 1993	Strain and stress principles of an electro-expulsive blanket